INTERNATIONAL JOURNAL FOR NUMERICAL METHODS IN FLUIDS
Int. J. Numer. Meth. Fluids 2004; **44**:545–578 (DOI: 10.1002/fld.657)

A 'poor man's Navier–Stokes equation': derivation and numerical experiments—the 2-D case

J. M. McDonough[1,*] and M. T. Huang[2]

[1]*Departments of Mechanical Engineering and Mathematics, University of Kentucky, Lexington, KY 40506-0503, U.S.A.*
[2]*Department of Electrical Engineering, University of Kentucky, Lexington, KY 40506-0046, U.S.A.*

SUMMARY

We present a systematic derivation of a discrete dynamical system directly from the two-dimensional incompressible Navier–Stokes equations via a Galerkin procedure and provide a detailed numerical investigation (covering more than 10^7 cases) of the characteristic behaviours exhibited by the discrete mapping for specified combinations of the four bifurcation parameters. We show that this simple 2-D algebraic map, which consists of a bilinearly coupled pair of logistic maps, can produce essentially any (temporal) behaviour observed either experimentally or computationally in incompressible Navier–Stokes flows as the bifurcation parameters are varied in pairs over their ranges of stable behaviours. We conclude from this that such discrete dynamical systems deserve consideration as sources of temporal fluctuations in synthetic-velocity forms of subgrid-scale models for large-eddy simulation. Copyright © 2004 John Wiley & Sons, Ltd.

KEY WORDS: turbulence; large-eddy simulation; subgrid-scale modelling; discrete dynamical systems

1. INTRODUCTION

Study of the logistic map,

$$m^{(n+1)} = \beta m^{(n)}(1 - m^{(n)}) \tag{1}$$

has a long history, and we shall not attempt an exhaustive review here; the well-known paper by May [1] provides considerable background as does the book by Collet and Eckmann [2]; a more concise introduction is given by Lauwerier [3] as a prologue to 2-D *discrete dynamical systems* (DDSs), and Alligood *et al.* [4] present elementary treatments of both the 1-D and

*Correspondence to: J. M. McDonough, Department of Mechanical Engineering, University of Kentucky, Lexington, KY 40506-0503, U.S.A.
†E-mail: jmmcd@uky.edu

Contract/grant sponsor: U.S. Air Force Office of Scientific Research; contract/grant number: F49620-00-1-0258
Contract/grant sponsor: NASA/EPSCoR; contract/grant number: wku 522653-00-10

Received 10 November 2001
Revised 26 August 2003

the 2-D cases. Feigenbaum [5] popularized the study of such systems with his discovery of universal constants related to the period-doubling bifurcations observed in a large class of quadratic maps. While none of these early studies attempted to make a direct connection with Navier–Stokes turbulence, the time series produced by the map iterations during chaotic behaviour were without doubt quite suggestive, as noted in Reference [1].

Possibly Pulliam and Vastano [6] were the first to indicate a likely direct connection: they observed that the bifurcation sequence of the 2-D Navier–Stokes (N–S) equations for flow over a NACA-0012 airfoil was very similar to that undergone by the logistic map, namely period-doubling bifurcations leading to chaos with increasing Reynolds number, and including 'periodic windows' within the chaotic regime. Frisch [7] goes further to demonstrate that a simple quadratic map (which can be easily transformed to (1)),

$$x^{(n+1)} = 1 - 2x^{(n)} \tag{2}$$

might be viewed as a '*poor man's Navier–Stokes equation*'. He carries this out in physical space with a simple *ad hoc* argument based on comparing terms of a rearrangement of (2) with those of the N–S equations. Clearly, one would not want to push this analogy too far since the N–S equations comprise a vector system of partial differential equations (PDEs), while Equation (2) is merely a single scalar algebraic expression.

In the following sections we will show, however, that multi-dimensional coupled versions of Equation (1) can be obtained in a straightforward way beginning with a Galerkin approximation of the N–S equations. In particular, we will arrive at the 2-D system of coupled logistic maps,

$$a^{(n+1)} = \beta_1 a^{(n)}(1 - a^{(n)}) - \gamma_1 a^{(n)} b^{(n)} \tag{3a}$$

$$b^{(n+1)} = \beta_2 b^{(n)}(1 - b^{(n)}) - \gamma_2 a^{(n)} b^{(n)} \tag{3b}$$

and then analyse some aspects of the behaviour of this system via numerical experiments. It will be shown that not only does this 2-D DDS undergo the usual logistic map bifurcation sequence, but that it also possesses additional regimes not seen in 1-D maps, analogous to those described in Abraham *et al.* [8] and elsewhere. These regimes, and the bifurcation sequences in which they are imbedded, are very much like those observed in laboratory experiments involving fluid flow and heat transfer (cf. Gollub and Benson [9]), and in many cases the corresponding time series are physically realistic. In fact, McDonough *et al.* [10] and Mukerji *et al.* [11] have demonstrated the ability to model both numerical simulations and experimental data with linear combinations of a slight modification of (1). This raises the question of whether algebraic expressions such as Equations (3) might be of value for producing practical, computational models of turbulence, e.g. in the context of subgrid-scale (SGS) models for large-eddy simulation (LES).

Indeed, the present study has been motivated by recent work on what is sometimes termed 'synthetic velocity' approaches to SGS modelling. In these procedures the subgrid-scale velocities are *directly modelled*, in contrast to modelling sub-grid stresses, as is typically done in LES. Examples of this can be found in recent papers by Domaradzki and Saiki [12], Kimmel and Domaradzki [13] and Scotti and Meneveau [14]. A related technique first proposed in McDonough *et al.* [15], and developed in Hylin [16] and Hylin and McDonough [17], employs such velocities directly, rather than as a means to construct subgrid-scale stresses,

making this approach somewhat similar to the nonlinear Galerkin and multilevel procedures of Temam and co-workers (see, e.g. Dubois *et al*. [18] and references therein). It is particularly within this framework that the results to be presented below might best be used, but there is potential for their application in any turbulence model that can be expressed in terms of small-scale fluctuating velocity components, possibly including even Reynolds-averaged Navier–Stokes (RANS) formulations.

In the context of the Hylin and McDonough [17] formalism, SGS velocity components are expressed as a product of three factors, *viz*. an amplitude, an anisotropy correction, and a temporally fluctuating component. The first two of these can be related to computed resolved-scale velocity (see Reference [17] for details), and algebraic chaotic maps (DDSs) have been proposed for the third factor. But no 'first-principles' derivation has previously been given to prescribe these maps. In the cited references linear combinations of the 1-D logistic map, and other related DDSs have been employed [16], but with no particular justification. One of the obvious shortcomings of these 1-D maps as models of N–S behaviour is their inability to produce quasiperiodic time series. On the other hand, it is well known that systems of 2-D maps often exhibit quasiperiodicities as well as phase lock and the related transitions between the two, as observed in the Rayleigh–Bénard convection experiments reported in Reference [9]. This suggests that the appropriate form of DDS should be at least two-dimensional, and it seems natural to employ a 2-D map to model the 2-D N–S equations (with the obvious extension to 3-D).

This paper documents an initial investigation of such a system. Our principle goal in this study has been to identify and characterize the possible behaviours of Equations (3) and to compare these, both qualitatively and quantitatively, to known behaviours of the N–S equations. We emphasize, however, that independent of results to be presented, Equations (3) arise from the 2-D equations, and any specific similarities to actual N–S -like behaviour must be considered within this framework.

The remainder of this work is organized as follows. In Section 2 we provide a detailed derivation of Equations (3), indicating the assumptions that are needed and the relationship of the bifurcation parameters to parameters that naturally occur in the N–S equations. Section 3 is devoted to the presentation and discussion of a fairly detailed (but also quite restricted—in the sense to be indicated below) regime map exhibiting the range of phenomena accessible by Equations (3). In Section 4 we summarize the results, draw conclusions, and speculate on the possible utility of coupled, multi-parameter DDSs of form (3) as subgrid-scale turbulence models.

2. ANALYSIS

In this section we derive the 'poor man's Navier–Stokes equation' given above as Equations (3), and then briefly discuss the relationships between these equations and other similar alternatives. We begin with the incompressible form of the Navier–Stokes equations,

$$\mathbf{U}_t + \mathbf{U} \cdot \nabla \mathbf{U} = -\nabla P + \nu \Delta \mathbf{U} \quad \text{for } (x,t) \in \Omega \times (t_0, t_f],\ \Omega \subseteq \mathbf{R}^d,\ d = 2,3 \tag{4}$$

which must be accompanied by the divergence-free constraint $\nabla \cdot \mathbf{U} = 0$ to provide a sufficient number of equations to obtain the pressure P and by appropriate boundary and initial conditions necessary to provide a well-posed problem. In Equation (4) $\mathbf{U} = (u, v)^{\mathrm{T}}$ is the velocity

vector in the 2-D domain Ω; v is kinematic viscosity, and ∇ and Δ are gradient and Laplace operators, respectively, in an appropriate co-ordinate system; the subscript t denotes partial differentiation with respect to time.

Mathematical analysis of Equations (4) often begins with a Leray projection to a divergence-free subspace of the Sobolev space of solutions (see, e.g. Constantin and Foias [19] for details), thus eliminating the pressure gradient from (4) when viewed in the weak sense. We will adhere to this herein. Thus, after typical scaling and application of the Leray projection, the 2-D N–S equations can be expressed as

$$u_t + uu_x + vu_y = \frac{1}{Re}\Delta u \tag{5a}$$

$$v_t + uv_x + vv_y = \frac{1}{Re}\Delta v \tag{5b}$$

which is actually a strong form representation—simply a 2-D system of Burgers' equations. In these equations subscripts indicate partial differentiation, and Re is the Reynolds number, $Re = UL/v$, with U and L being appropriate velocity and length scales, respectively. We remark that Equations (5) arise frequently in CFD as the first step in implementing projection methods of the form considered by, e.g. Gresho [20].

We now construct a Fourier representation of u and v:

$$u(x,t) = \sum_{k=-\infty}^{\infty} a_k(t)\varphi_k(x) \tag{6a}$$

$$v(x,t) = \sum_{k=-\infty}^{\infty} b_k(t)\varphi_k(x) \tag{6b}$$

Here $k \equiv (k_1, k_2)^{\mathrm{T}}$ is a 2-D wave vector. We will assume the tensor product basis set $\{\varphi_k\}$ is complete (in the norm of an appropriate Sobolev space), orthonormal, divergence-free, and in C_0^∞ and exhibiting properties analogous to complex exponentials with respect to differentiation. These assumptions make the following derivation particularly simple, and not all are absolutely necessary. At the same time, it should be recognized that actually constructing such a basis set for computational purposes could be difficult; but this is not necessary for the present analysis. We will give details for the x-momentum equation; treatment of the y-momentum equation is identical.

Application of the Galerkin procedure in the usual way results in an infinite system of ordinary differential equations (ODEs) for the Fourier coefficients in representation (6); e.g. for x-momentum we have

$$\dot{a}_k = -\sum_{\ell,m} A^{(1)}_{\ell m,k}\, a_\ell a_m - \sum_{\ell,m} A^{(2)}_{\ell m,k}\, a_\ell b_m - \frac{C}{Re}|k|^2 a_k, \quad -\infty < |k| < \infty \tag{7}$$

In Equation (7) $A^{(i)}_{\ell m,k}$, $i = 1,2$, arise from Galerkin triple products, and it is assumed that any required normalizations have been absorbed; C is a normalization constant arising from the fact that although the $\{\varphi_k\}$ may be orthonormal, this is not necessarily true for their derivatives. In particular, we are assuming that the derivatives are orthogonal, but with possibly different normalizations.

We might view Equation (7), and the corresponding equations for the b_k, as an infinitely accurate shell model (see Bohr *et al.* [21], and references therein) suggesting that we should proceed by deleting from consideration all but some finite number of wave vectors k. In fact, we will remove *all but a single arbitrary* wave vector. This results in

$$\dot{a} = -A^{(1)}a^2 - A^{(2)}ab - \frac{C}{Re}|k|^2 a \tag{8a}$$

$$\dot{b} = -B^{(1)}b^2 - B^{(2)}ab - \frac{C}{Re}|k|^2 b \tag{8b}$$

Equations (8) constitute a fairly simple pair of non-linear ODEs, and it should be evident that the same analysis starting with the 3-D N–S equations would result in an additional equation, and a further coupling term in each equation; hence, extension to 3D is direct.

It is straightforward to solve this system numerically. Here we will employ a simple forward Euler single-step, explicit time integration procedure. This leads to

$$a^{n+1} = a^n - \tau\left[\frac{C}{Re}|k|^2 a^n + A^{(1)}(a^n)^2 + A^{(2)}a^n b^n\right] \tag{9a}$$

$$b^{n+1} = b^n - \tau\left[\frac{C}{Re}|k|^2 b^n + B^{(1)}(b^n)^2 + B^{(2)}a^n b^n\right] \tag{9b}$$

where τ is an arbitrary discrete time step parameter. We now rearrange the first of these equations as

$$a^{n+1} = \tau A^{(1)}a^n\left(\frac{1 - C\tau|k|^2/Re}{\tau A^{(1)}} - a^n\right) - \tau A^{(2)}a^n b^n \tag{10}$$

It is easily seen at this point that if we are to recover the logistic map we must require

$$\frac{1 - C\tau|k|^2/Re}{\tau A^{(1)}} = 1 \tag{11}$$

which implies that

$$\tau A^{(1)} = 1 - \frac{C}{Re}\tau|k|^2 \tag{12}$$

This, in turn, permits us to write (10) as

$$\begin{aligned} a^{n+1} &= \left(1 - \frac{C}{Re}\tau|k|^2\right)a^n(1 - a^n) - \tau A^{(2)}a^n b^n \\ &= \beta_1 a^n(1 - a^n) - \gamma_1 a^n b^n \end{aligned} \tag{13}$$

with obvious definitions of β_1 and γ_1.

It is clear that if we suppress the coupling (i.e. set $\gamma_1 = 0$), then we recover the form of the usual logistic map, Equation (1). Furthermore, it is easily seen that as $Re \to \infty$, $\beta_1 \to 1$ from below. Since $f(a) \equiv a(1-a)$ has a maximum of 1/4 for $a \in [0, 1]$ we see that we should

rescale β_1 by a factor of 4 to obtain the usual unit scaling typical for DDSs as was done in Reference [1]. This then suggests that the range of values for β_1 is between zero and four, just as in the logistic map. It is also worth observing that β_1 depends on the wavevector magnitude, and on the numerical time step parameter. In particular, we see that the product of these factors must be less than Re/C in order for $\beta_1 > 0$ to hold. This implies that as the wavevector magnitude increases, the time step size must decrease, just as would certainly be the case in order to maintain stability of an explicit time-stepping method such as forward Euler. It has recently been shown in McDonough *et al.* [22], however, that a fairly wide range of stable behaviour occurs even when $\beta < 0$ holds.

A completely analogous derivation applied to Equation (9b) results in a coupled system of two logistic maps, obtained directly from the N–S equations:

$$a^{(n+1)} = \beta_1 a^{(n)}(1 - a^{(n)}) - \gamma_1 a^{(n)} b^{(n)} \tag{14a}$$

$$b^{(n+1)} = \beta_2 b^{(n)}(1 - b^{(n)}) - \gamma_2 a^{(n)} b^{(n)} \tag{14b}$$

We also see that $\gamma_1 = \tau A^{(2)}$ (and analogous to this, $\gamma_2 = \tau B^{(2)}$), indicating that it is basically set by the time-stepping parameter and the Galerkin triple product corresponding to the selected wavevector. The latter of these carries information associated with the velocity gradients. It is straightforward to check (by constructing the Galerkin triple products) that $A^{(2)}$ is related to u_y, and $B^{(2)}$ arises from v_x in Equations (5). Of course this relationship is somewhat complicated by details of wavevector dependence of the triple products, and we have lumped this into the bifurcation parameters γ_1 and γ_2. By determining valid ranges for these parameters (as a function of the βs) as we will do in the present study, we will have taken a first step toward constructing a mapping of flow physics (the velocity gradient tensor) to model parameters.

The four parameters appearing in this 2-D DDS are all associated with nonlinear (or, at least bilinear) terms, and we would expect the possibility of bifurcations with respect to each one, separately. Because the present investigation of this system will be entirely numerical, we will consider only a rather small subspace of the complete four-dimensional space of parameter values $(\beta_1, \beta_2, \gamma_1, \gamma_2)$. This will render the results easier to interpret, and as we now argue, our choice will be a natural one. In particular, since Equations (14) arose from the N–S equations, and, β_1 and β_2 both have the same relationship with the Reynolds number, it is reasonable (but not necessarily correct—see Reference [22]) to set $\beta_1 = \beta_2$. It is less clear that also setting $\gamma_1 = \gamma_2$ is even a natural choice. But we have done so for simplicity in this initial study, while recognizing that there may be important phenomena omitted as a consequence. In any case, we will select our bifurcation parameter values from along a diagonal of the 4-D curvilinear parallelopiped $[0, \beta_{1,\max}] \times [\gamma_{1,\min}, \gamma_{1,\max}] \times [0, \beta_{2,\max}] \times [\gamma_{2,\min}, \gamma_{2,\max}]$ by setting $\beta_2 = \beta_1$ and $\gamma_2 = \gamma_1$.

We remark that although Equations (14) are relatively simple in structure, the mathematical theory of systems of polynomials is difficult. In part because of this, analytical theory of multi-dimensional DDSs is still in its infancy despite a very long history as indicated, e.g. in Abraham *et al.* [8]. The first such map to receive wide attention in the modern literature was that due to Hénon [23], which was constructed as an algebraic model of the Lorenz equations [24]. As is well known, these equations are, themselves, a very crude (but differential) model of the N–S equations plus the thermal energy equation (cf. Yorke and Yorke [25]), and while

they retain some of the features of the N–S equations for very specific flows (e.g. flow in a toroidal thermosyphon [25]), they cannot be viewed as a useful model in general. Moreover, although similarities between iterations of the DDS presented in Reference [23] and solutions to the Lorenz equations are claimed, in fact details of the bifurcation sequences show little similarity (but see Hénon and Pomeau [26]).

Several other 2-D DDSs are studied (numerically) in Reference [8], as well as in Frøyland [27], where some analytical results also are presented. But in all these cases the basic system structure is similar in that one of the two equations is always strictly linear. As a consequence there is no 'symmetry of structure' that we would expect to find in models of the N–S equations, and which is evident in our Equations (14). We also note that Equations (14) is not the only possible DDS that can be obtained from the N–S equations by a Galerkin procedure. It would be possible, for example, to retain the pressure gradient terms (i.e. not invoke a Leray projection) and introduce a constant forcing in the Fourier space representation, Equation (7), analogous to the treatment given in McDonough and Bywater [28] for Burgers' equation. Of course, this would not result in a DDS in the form of a pair of logistic maps. Alternatively, we could, after retaining the pressure gradient in the basic formulation, eliminate it algebraically in Fourier space as is often done for spectral approximations of the N–S equations. Finally, we emphasize that the specific constraint, Equation (11), was *necessary* for obtaining a coupled system of logistic maps, but even without this we would still have produced a reduced shell model related to the N–S equations. Indeed, we have performed numerical experiments with some of these formulations and have found their generic behaviours to be similar to those reported herein. But we also have found that such systems exhibit far smaller regions of non-divergent behaviour making them less suitable for application to the modelling procedures we propose.

3. RESULTS AND DISCUSSION

In this section we present results obtained by iterating the DDSs of Equations (14) for various values of $\beta_1 = \beta_2 = \beta$ and $\gamma_1 = \gamma_2 = \gamma$ in the range $\beta \in [1,4]$, $\gamma \in [\gamma_{\min}(\beta), \gamma_{\max}(\beta)]$. We will first characterize the different regimes that have been identified by means of their power spectra, and then summarize the behaviour in the form of a regime map analogous to that presented in Reference [28] in a somewhat similar study of a forced Burgers' equation. This will provide a broad overview of the range of behaviours exhibited by Equations (14), and at the same time at least a qualitative comparison with what is known regarding possible regimes, and transitions between these regimes, for N–S flows. Following this we present more details of representative behaviour from within each of the regimes in the form of time series, phase portraits, autocorrelations, cross correlations, flatness and skewness.

Most calculations reported for this study were performed in parallel mode using OpenMP with eight processors on a HP N-4000 96-processor symmetric multiprocessor at the University of Kentucky Computing Center. Additional computations were carried out on a HP J-2240 workstation in the Computational Fluid Dynamics Laboratory, also at the University of Kentucky. All results were obtained using double precision (64-bit) Fortran. A typical run consisted of 5×10^4 iterations ($\sim$ time steps) of Equations (14) with the last 10^4 subjected to the indicated statistical analyses, except in the case of power spectra. In this case a standard

radix-2 FFT was used, and this was applied to the final 8192 points of the time series for $\{a^{(n)}\}$.

3.1. Solution regimes

One of the most interesting outcomes of this study was the identification of numerous regimes of temporal behaviour, including all of those found for the 1-D logistic map, as well as several other important N–S regimes often seen in laboratory experiments. We have made these identifications entirely in terms of the power spectral density (psd), and a few comments regarding this choice are in order.

Especially in the context of chaotic solutions, fractal dimension in one form or another (e.g. the correlation dimension of Grassberger and Procaccia [29]) or Lyapunov exponents (see, e.g. Wolfe *et al.* [30]) have been widely used. Both of these, as well as various related quantities, are computationally intensive and their construction cannot always be carried out in a completely automatic, objective fashion. As we will indicate in more detail below, $\mathcal{O}(10^7)$ realizations of Equations (14) will be computed, and the effort required to employ either fractal dimension or Lyapunov exponents as a characterization technique is quite prohibitive, especially in terms of human time expenditure needed to provide complete confidence in the results. Furthermore, it is not clear how to use either of these quantities to distinguish specific chaotic behaviours of the types we will describe in the sequel, although further investigations of this could be worthwhile. We also note the fairly intuitive result in Reference [10] that no single statistical quantity could adequately represent chaotic behaviour. The power spectrum, however, was not used in that study, and probably would not have been appropriate in the context of fitting dynamical systems to data, the focus of the work reported there (but see Reference [11]). Thus, we recognize at least some possible shortcomings with this approach, but in general we find it works well.

In the present case we are seeking only identification, and not quantification in the sense of curve fitting. Thus, the psd appears to be adequate (with a few exceptions noted below), and it is very efficient and automatic. We begin by providing a list of the types of behaviour we have identified in the time series of Equations (14) using this technique: (i) steady, (ii) periodic, (iii) periodic with different fundamental frequency, (iv) subharmonic, (v) phase locked, (vi) quasiperiodic, (vii) noisy subharmonic, (viii) noisy phase locked, (ix) noisy quasiperiodic with fundamental, (x) noisy quasiperiodic without fundamental, (xi) broadband with fundamental, (xii) broadband with different fundamental, (xiii) broadband without fundamental, (xiv) divergent.

It is important to note that the attribute 'noisy' implies some broadband aspects in the psd, but we use it here in conjunction with some other attribute which is taken to be the dominant feature. It seems unclear to what extent this might be applied to experimental data because of ubiquitous instrumentation noise. In the case of a numerically evaluated DDS there is no such noise, and the broadband features of the psd reflect actual behaviour of the DDS. One consequence of this in any of the listed cases is at least mild sensitivity to initial conditions (SIC), commonly viewed as the hallmark of a *strange attractor*. We will discuss what is meant by 'mild' in the context of time series and autocorrelations, below. We also observe that presence of the fundamental frequency in the power spectrum tends to suppress SIC, even in the case of a broadband spectrum. Because of this, noisy periodic and broadband with fundamental are indistinguishable. Furthermore, we include in phase locked

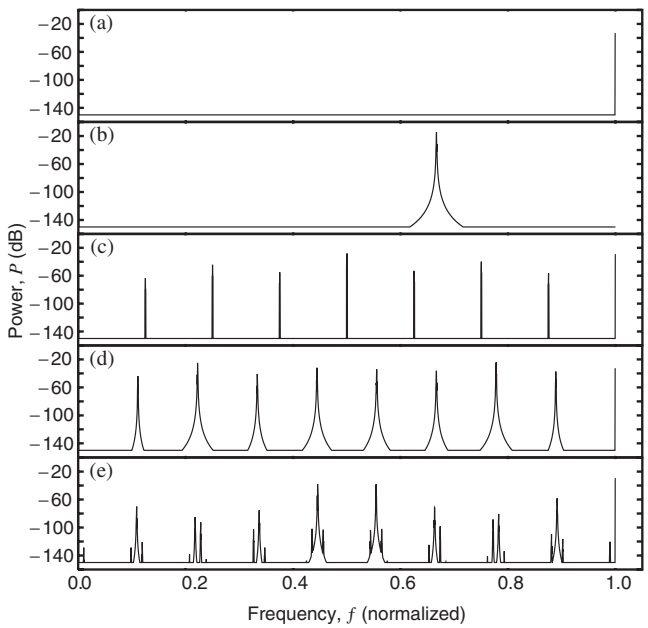

Figure 1. Non-noisy power spectra: (a) periodic ($\beta = 3.1, \gamma = -0.05$); (b) periodic with different fundamental ($\beta = 3.84, \gamma = -0.05$); (c) subharmonic, three bifurcations ($\beta = 3.57, \gamma = -0.02$); (d) phase locked ($\beta = 2.6, \gamma = -0.655$); and (e) quasiperiodic ($\beta = 3.1, \gamma = -0.25$).

the case of n-periodic ($n > 2$) independent of whether the fundamental is present. But we note that distinguishing subharmonic behaviour beyond the first bifurcation from a phase lock is difficult without knowing the sequence of behaviours leading to the given state as a bifurcation parameter is varied. Our approach has been to characterize the behaviour as subharmonic if the following criteria are met: (i) number of frequencies n_f is a power of two; i.e. there exists an integer m such that $n_f = 2^m$, and (ii) the power of all frequencies at the 2^{m-1} level is less than that of either of their nearest neighbours (in frequency) at the 2^m level. Otherwise, the behaviour is classified as phase locked when such a distinction is necessary. The same criteria are applied to the corresponding noisy cases.

We also remark that it is tempting to associate divergent behaviour with simply employing a numerical time step that is too large. Recall, that there is a numerical time step factor τ in Equations (9) appearing in the construction of our bifurcation parameters. But, in some respects this is incidental, and discrete quadratic maps tend to exhibit divergent behaviour in certain ranges of values of their bifurcation parameters independent of the method of their derivation. Thus, we prefer to not associate divergence with numerical instability, *per se*.

Figure 1 displays psds in order of increasing complexity for examples of each of the above 'non-noisy' classifications except steady (which is trivial) and divergent, which is non-stationary (the values of the time series go to infinity, usually very rapidly). Each of these psds has a sharp peak at zero frequency since we did not remove the average ('dc component'), but this cannot be seen in the plots. Also note that the frequencies shown have been normalized because the time increments corresponding to map iterations are arbitrary. In part (a) of the

figure we see a single additional sharp peak at the highest possible frequency; this is the basic periodic case. In continuous dynamical systems the transition from steady to periodic usually occurs via a Hopf bifurcation, but here in the DDS case this corresponds to a 'pitchfork' bifurcation (named for its appearance in the bifurcation diagram of the 1-D map). Part (b) of the figure displays a periodic case with frequency different from the original fundamental frequency, and part (c) shows a subharmonic case that has undergone three bifurcations. Figure 1(d) shows a phase-locked behaviour, and in part (e) we present a simple quasiperiodic case, which like its continuous counterpart occurs as the result of a (second, in the continuous case) Hopf bifurcation. We comment that in terms of an actual bifurcation sequence, part (e) would initially precede part (d), as we now discuss.

Once quasiperiodicity begins as a bifurcation from a periodic state, it is possible that further changes in the bifurcation parameter will make the two incommensurate frequencies of this case again commensurate. That is, if f_1 and f_2 are two frequencies satisfying $f_1/f_2 = p_1/p_2$, p_1/p_2 irrational, then as β and/or γ are (is) varied it is possible for the frequency ratio to change such that $f_1/f_2 = q_1/q_2$, with q_1/q_2 rational. Then $q_2 f_1 = q_1 f_2$ is the 'locking' frequency. In the discrete case, if f_1 is the fundamental, then $q_2 < q_1$ must hold; hence, the locking frequency is less than the fundamental, and all frequencies appearing in the psd (including the original fundamental, f_1) are harmonics of the locking frequency. Part (d) of Figure 1 is a case of this. In the physics literature this is often termed *resonance*, and the frequency ratios are referred to as *winding numbers*. It is well known from the nonlinear dynamics literature (see, e.g. Reference [27]) that rational winding numbers give rise to Arnol'd 'tongues' in regime descriptions depicting quasiperiodic and phase-locked (resonant) behaviours.

In Figure 2 we display psds of the noisy cases. Figure 2(a) presents the case of a noisy subharmonic. The spectral peaks are well defined and rise tens of decibels (dB) above the noise; thus, they are easily detected. It is important to again note, however, that the noise is an inherent feature of the underlying attractor, and we conjecture that at least some 'noise' seen in experimental data may well be of this sort. In part (b) of the figure we show the case corresponding to a noisy phase lock. Again, the spectral peaks are easily identified. The noisy quasiperiodic case with fundamental frequency still present is displayed in Figure 2(c). We comment that as bifurcation parameters are changed to move the system deeper into the noisy regime, recognizing spectral peaks becomes increasingly more difficult. The corresponding case without the fundamental frequency is shown in part (d) of the figure. We will later see that these two cases can also be readily distinguished from corresponding broadband behaviour by their autocorrelation functions.

The remaining three cases involve broadband behaviour, with and without the fundamental frequency and with a fundamental that is lower than the maximum resolved frequency. There is clearly some subjectivity in deciding whether there are any remaining identifiable peaks (even the fundamental) in some cases, and we have consistently imposed the somewhat arbitrary requirement that there be no peaks rising to 20 dB or more above the background noise for a signal to qualify as broadband w/o fundamental. As we indicated earlier, even though the spectrum may be nearly white noise, if the fundamental remains then various other statistics are similar to those of quite regular behaviour; e.g. the autocorrelation does not decay rapidly.

In concluding this subsection we remark that the 12 different behaviours indicated in Figures 1 and 2 are clearly distinct, although as we have already noted there can be some ambiguity in a few specific situations. Thus, in constructing the regime maps to be displayed

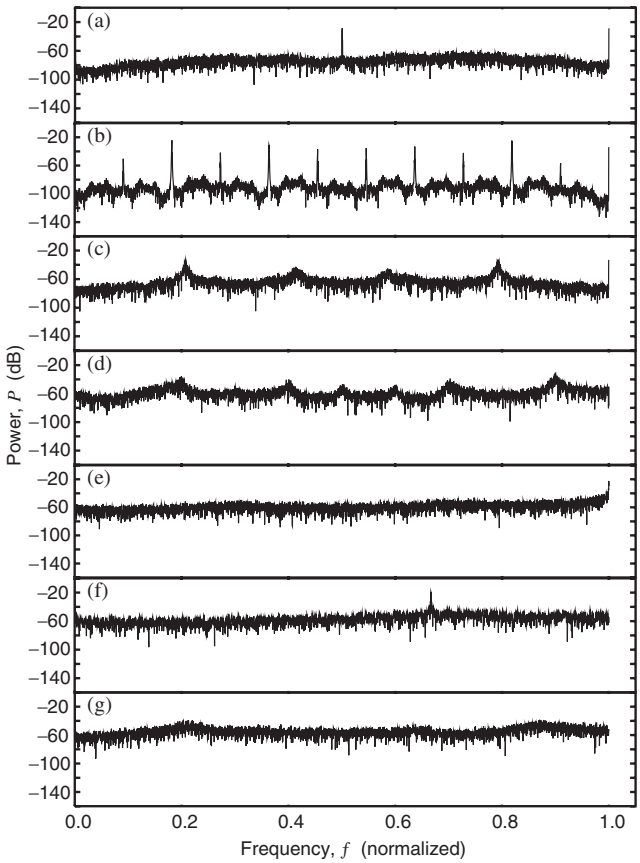

Figure 2. Noisy power spectra: (a) subharmonic ($\beta = 3.6, \gamma = -0.1$); (b) phase locked ($\beta = 2.2, \gamma = -0.825$); (c) quasiperiodic w/fundamental ($\beta = 2.5, \gamma = -0.7$); (d) quasiperiodic w/o fundamental ($\beta = 2.3, \gamma = -0.8002$); (e) broadband w/fundamental ($\beta = 3.2, \gamma = -0.331$); (f) broadband w/different fundamental ($\beta = 3.83, \gamma = -0.0678$); and (g) broadband w/o fundamental ($\beta = 2.5, \gamma = -0.74$).

and discussed in the next subsection, we have used this classification to build a basic pattern recognition algorithm that automatically assigns a behaviour of one of the above types (and a corresponding numerical value) for any arbitrary psd.

3.2. The regime map

Plate 1 displays a summary of the results of this study in the form of a regime map (a 2-D bifurcation diagram) in part (a), indicating regions of a specific type of behaviour as a function of β and γ. Data plotted here were produced completely automatically using an 'image processing' algorithm described elsewhere that assigns a numerical value to each type of power spectrum, as indicated in part (b) of this figure. Computations were performed with a (β, γ)-resolution corresponding to $\Delta\beta = \Delta\gamma = 0.00125$, resulting in 3.456×10^6 separate cases. As noted above, each run consisted of a minimum of 5×10^4 map iterations of Equations

(14). Such large numbers of iterations were deemed necessary when it was discovered that the initial transient could last beyond 2×10^4 iterations if (β, γ) corresponded to a point near a regime boundary (i.e. a bifurcation point). The same initial map values were used in all calculations from which the regime map was constructed: $a^{(0)} = 0.3$, $b^{(0)} = 0.95$, henceforth termed 'standard'. There was no particular rationale for this choice. Because there is no uniqueness theorem in multidimensions, we often ran various other initial conditions and, indeed, we sometimes discovered multiple attractors. We will provide limited further discussions for particularly interesting cases in the sequel, and in additional work currently in progress; but we note that existence of multiple attractors is well known for 2-D maps (see, e.g. Reference [27] and Bible and McDonough [31]).

Part (b) of Plate 1 displays the colour table with regime descriptions and numerical assignments for each regime, provided to aid discussions of the regime map in Part (a) of the figure. We first remark that for $\beta \leqslant 1.0$ solutions are always either steady (actually null, as in the 1-D case) or divergent. Obviously, neither of these states is of interest from a modelling standpoint, so we will give no further consideration to the regimes corresponding to $\beta \leqslant 1.0$. It is also clear that these two states cover much of the regime map for $\beta > 1.0$ as well, but in this case there is still a very significant area in which 'interesting' behaviour occurs.

In further elaborating on the nature of the regime map we first observe that the β axis $(\gamma = 0)$ shows the bifurcation sequence of the usual 1-D logistic map, Equation (1),

$$\text{steady} \rightarrow \text{periodic} \rightarrow \text{subharmonic} \rightarrow \text{chaotic}$$

as it must. In particular, Equations (14) collapse to two uncoupled 1-D logistic maps when $\gamma = 0$, and a well-known theorem for 1-D maps shows that the regimes are unique. Thus, even though $b^{(0)} \neq a^{(0)}$, the ultimate stationary state will be the same for each map. Also note that other behaviours (not usually identified as part of the logistic map bifurcation sequence) appear to be indicated beyond $\beta \simeq 3.5$. This occurs because, as already shown in Figure 2, we have identified numerous additional states, any one of which might simply be called chaotic, but which exhibit distinct power spectra.

It is interesting that non-steady behaviour can occur in 2D at values of β only slightly larger than the value at which nontrivial steady solutions begin in 1D. In the region to the left of onset of periodicity in the 1-D case ($\beta \leqslant 3.0$), the basic bifurcation sequence corresponding to *decreasing* γ with β fixed is

$$\text{steady} \rightarrow \text{periodic} \rightarrow \text{quasiperiodic} \rightarrow \text{chaotic}$$

the Ruelle and Takens [32] bifurcation sequence for the N–S equations. We comment at this time that we will employ the term 'chaotic' somewhat loosely herein, but in any case associate it with behaviour exhibiting at least 'mild' sensitivity to initial conditions (SIC) and irregular appearance of the time series. (Mild SIC will be discussed in more detail below in the context of time series where it can be easily identified.) As already noted, there are numerous states embedded in this sequence, as can be seen more clearly in the zoomed views provided in Plate 2. (We note that these figures were not produced by merely zooming the graphics display window. Instead, the calculations were repeated over the displayed restricted regions with $\Delta\beta = \Delta\gamma = 0.000625$.) Here, numerous Arnol'd tongues of phase-locked behaviour are evident, along with a large number of regions of noisy quasiperiodicity and noisy phase lock preceding the regimes corresponding to broad-band power spectra, which themselves contain regions of quasiperiodicity and phase lock—both non-noisy and noisy.

It is also suggestive from Plates 2(a) and (b) that the boundaries separating these regimes are sometimes fractal. We will not attempt to rigorously demonstrate this herein beyond providing the inset to Plate 2(a) which displays a (graphics) zoom-in of the region $(\beta, \gamma) \in [3.2075,\ 3.2275] \times [-0.355, -0.335]$. This shows the (apparently) fractal nature of boundaries between noisy quasiperiodic states with, and without, the fundamental frequency. In general, Plates 1 and 2 suggest that (for fixed initial data) the regime boundaries (locus of bifurcation points) are nonfractal provided one of the two (non-divergent) states approaching the boundary is not noisy; otherwise, the boundary appears to be fractal.

Beginning immediately with $\beta > 3.0$, steady behaviour is no longer observed; but the remaining states of the Ruelle and Takens sequence persist until $\beta = 3.208$ where a reverse bifurcation back to periodicity occurs at $\gamma = -0.3$. The γ interval over which this takes place expands with increasing β until $\beta \simeq 3.29$, after which only periodic behaviour is seen until the subharmonic [5] bifurcation sequences begin in the range $\beta \in [3.355, 3.445]$, the precise value depending on γ.

There are several other features of Plates 1 and 2 that are of general interest, more from the standpoint of dynamical systems than in the context of SGS turbulence models *per se*. The most pervasive of these is a large region of periodicity beginning at $\beta \simeq 3.639$ and extending as far as $\beta \simeq 3.935$ (modulo 'holes' and 'islands', to be discussed below) having bounds on γ ranging from ~ 0.18 to ~ 0.5, with exact values depending on β. This region, which we term 'high-β periodic,' is connected to the main region of periodicity by a 'bridge of periodicity,' as can be seen in Plates 1(a) and 2(b). We note, however, that existence and extent of this bridge depends on initial conditions, as can be seen from Plate 3. This figure was prepared exactly as was Plate 1(a), but employing slightly different initial conditions: $a^{(0)} = 0.31,\ b^{(0)} = 0.94$, which will be termed 'alternative' in the sequel. In this case the bridge does not completely connect the two periodic regions, indicating existence of at least two solutions to the DDSs Equations (14) in the region $\beta \in (3.4, 3.6)$. On the other hand, the large region of periodicity at higher values of β still persists, and is probably generic for Equations (14). It should be noted, however, that this region contains very small islands (sometimes single isolated points to within our computational resolution) of various other behaviours that cannot be displayed at the plotting resolution employed herein. The inset to Plate 2(b), a graphics zoom-in, provides an example.

Another prominent feature that appears adjacent to periodic and quasiperiodic regions, but embedded within divergent states is a series of islands (see Abraham *et al.* [8]) where the DDS remains bounded even though it is divergent at most nearby (β, γ) points. Often interspersed with these are holes: regions of divergence completely surrounded by bounded behaviour. These regions can be seen in Plates 2(a,b) for $\gamma < 0$ with β in the neighbourhood of 3.3–3.6, and for $\gamma > 0$ and β near 3.9, respectively. We see from these figures that islands occur only for states retaining a fundamental frequency.

It is important to note other significant differences between Plates 1(a) and 3 arising from SIC. First, careful comparison of these two figures shows that onset of divergence occurs at a higher value of (positive) γ in Plate 3; hence, the corresponding initial conditions lead to a larger region of stable behaviour. Second, the regime boundaries in the neighbourhood of $\beta \simeq 3.2, \gamma \simeq -0.3$ are completely different, as is the topology of the hole-island structure near $\beta \simeq 3.5, \gamma \simeq -0.4$ and $\beta \simeq 3.9, \gamma \simeq 0.4$. It will be essential for the construction of SGS models to more completely understand the effects of changing initial conditions.

In summary, the regime maps displayed in Plates 1–3 indicate existence of two main bifurcation sequences: (i) Ruelle and Takens, and (ii) Feigenbaum. But in most cases of either fixed β or fixed γ with the opposite parameter varied, the sequence is far more complicated (as seems to also occur in physical experiments—see, e.g. Reference [9]). Moreover, we have found evidence of intermittency as well, to be discussed in the next subsection in the context of time series and phase portraits where it is more easily identified.

3.3. Time series

In this subsection we present time series for each of the important classes of behaviour already discussed in terms of psds; we also provide phase portraits for particularly interesting cases. In addition, we give a definition of 'mild SIC' alluded to earlier, and we display evidence of intermittent behaviour for the DDS of Equations (14).

Figure 3 presents time series for each of the possible states shown in Plates 1–3 (except steady and divergent), and whose power spectra have been provided in Figures 1 and 2. The time scale used is arbitrary (it would be set with estimates of physical time scales in a complete model), but the same scale is used in all time series presented herein. From the standpoint of constructing models, it might at first seem dismaying that such a large number of characteristic behaviours can occur in very close proximity in parameter space, and in some cases seemingly inextricably entangled (recall inset to Plate 2(a)). But one should first raise the question whether this actually can occur spatially and/or temporally in N–S flows. At present there seems to be no experimental evidence to either support or refute this behaviour, but if it should be confirmed, then the structure apparent in the regime maps presented here would be an advantage for models.

There are several interesting aspects of the data displayed in Figure 3. First, it can be seen that parts (c), (e) and (f) of the figure show very similar features. These correspond to subharmonic after three bifurcations ($\beta = 3.57, \gamma = -0.02$), quasiperiodic ($\beta = 3.1, \gamma = -0.25$) and noisy subharmonic ($\beta = 3.6, \gamma = -0.1$), respectively. Their corresponding power spectra are distinctly different, as can be seen from Figures 1 and 2. It might at first seem surprising that noisy subharmonic behaviour would appear so similar to the two states having non-noisy spectra. But from Figure 2(a) we see that the noise is at very low power compared with the fundamental and subharmonic, and the overall effect seems similar to the 'scrambling' that occurs due to incommensurate frequencies in the quasiperiodic case. Furthermore, the non-noisy subharmonic case of Figure 1(c) is only a few bifurcations away from chaos and is beginning to show noticeable complexity.

The second observation concerns strong similarities among Figures 3(d), (g)–(i). These correspond to phase locked, noisy phase locked, noisy quasiperiodic w/fundamental and noisy quasiperiodic w/o fundamental; their power spectra have been presented in Figure 1(d) and Figures 2(b)–(d), respectively. It is of interest to note that these four states appear mixed with one another over significant portions of the regime maps (e.g. again recall the inset to Plate 2(a)), and while this fact raises serious concerns regarding the structure of models in these regimes, the time series (the ultimate output of the model) are very similar. Indeed, without the detailed power spectral analyses we have performed in this study one might not recognize that distinct states exist, so this mix of regimes will likely have only minimal effect on models. Finally, we note the essentially identical time series in Figures 3(b) and (k). This is at first very surprising when one considers the corresponding power spectra presented in

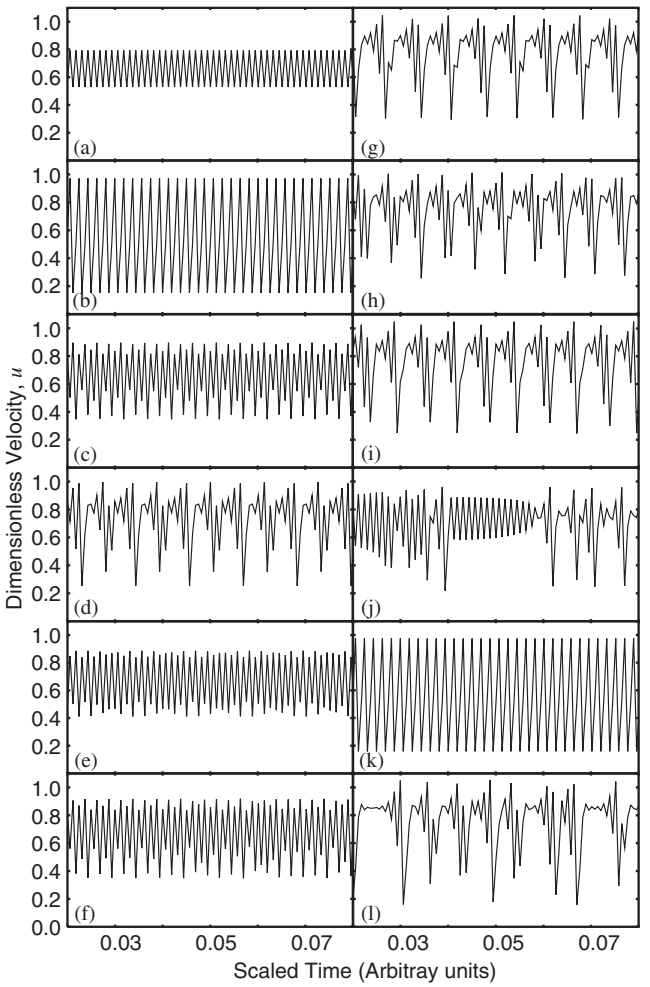

Figure 3. Time series for all nontrivial states: (a) periodic; (b) periodic with different fundamental; (c) subharmonic; (d) phase locked; (e) quasiperiodic; (f) noisy subharmonic; (g) noisy phase lock; (h) noisy quasiperiodic w/fundamental; (i) noisy quasiperiodic w/o fundamental; (j) broadband w/fundamental; (k) broadband w/different fundamental; and (l) broadband w/o fundamental.

Figures 1(b) and 2(f), respectively. Figure 3(k) is a particularly interesting case that will be treated in more detail later in this section.

We earlier alluded to a property we term 'mild SIC'. In Figure 4(a) we display time series from a case exhibiting this property corresponding to $(\beta, \gamma) = (3.7, 0.1)$. The two time series $\{a^{(n)}\}$ shown in the figure correspond to initial conditions $a^{(0)} = 0.3,\ b^{(0)} = 0.95$ (black) and $a^{(0)} = 0.31,\ b^{(0)} = 0.94$ (grey). There are two key features to observe in these plots. First, the amplitudes of the two time series are unequal from point to point, and they do not vary in a synchronous way; i.e. one time series cannot be obtained from the other by a phase shift. But despite this, we observe the second main feature: the phase difference between the two time

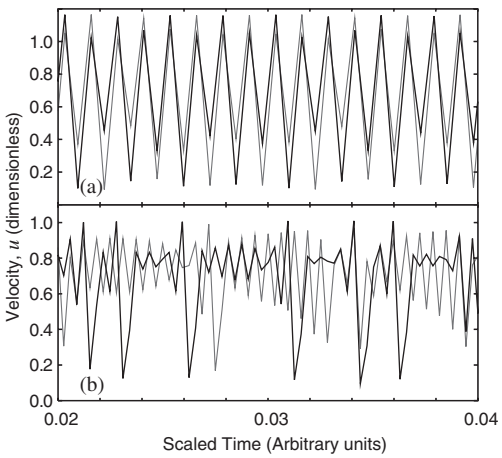

Figure 4. Depiction of *mildly* SIC; black lines from standard initial conditions, grey lines from alternative conditions: (a) time series showing mild SIC; and (b) time series showing SIC.

series remains unchanged (in phase, for this case). We use these properties to define *mild sensitivity to initial conditions*. It should be noted that these time series appear to be chaotic, and their power spectra are noisy quasiperiodic. On the other hand, both the fundamental and a subharmonic mode are of significant amplitude. We have found that if the fundamental is present, SIC will often be no more than mild; conversely, once the fundamental disappears true SIC occurs. An example of this latter case is displayed in part (b) of Figure 4, corresponding to $(\beta, \gamma) = (3.2, -0.415)$ to clearly indicate the differences. Here, we see the time series going in and out of phase as they evolve in time. But it is not always the case that existence of the fundamental is sufficient to guarantee mild SIC, and we have been unable to find a property that provides completely certain prediction of this, other than Lyapunov exponents.

We next consider the situation concerning intermittency. It should first be noted that the term *intermittency* has a more precise meaning in the context of dynamical systems than is the case for physical turbulence. In particular, there are at least three identified types of intermittency (see Bergé *et al*. [33]) associated with the manner in which Floquet exponents cross the unit circle, and at least two of these have been found in physical settings. On the other hand, physical turbulence is usually characterized by a value of the *intermittency factor*, defined (heuristically) as the ratio of the time a flow is turbulent to the total time of measurement; and also related to the asymptotic behaviour of the *flatness* of small scales as the high-pass filter frequency applied to the data increases (see Frisch [7]). We observe that it does not seem possible to detect intermittency from a power spectrum, but it is relatively easy to identify it in a time series; and at least for type I intermittency, it is fairly easy to deduce its onset from a phase portrait. We will employ both the time series and phase portraits in what follows.

Figure 5(a) displays time series of both u and v components of the dynamical system in a state corresponding to the onset of type I intermittency. (We will use this notation interchangeably with $\{a^{(n)}\}$ and $\{b^{(n)}\}$.) The associated phase portrait is presented in Figure 5(b). From the time series we see periods of low amplitude, fairly regular oscillation superimposed on a signal of growing mean amplitude followed by a burst of high-amplitude, less regular

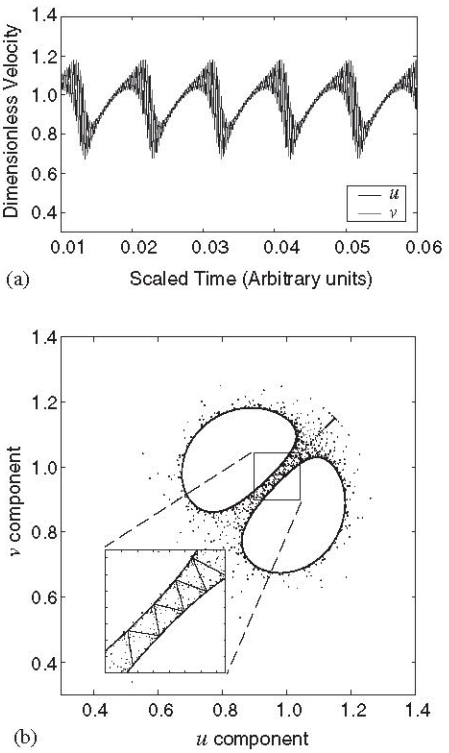

Figure 5. Description of Type I intermittency; $(\beta,\gamma)=(1.1,-1.013)$. (a) time series; (b) phase portrait.

behaviour. The two separate limit cycles apparent in part (b) of the figure are characteristic of (discrete) quasiperiodic behaviour, and for low β and low (in magnitude) γ these are small in radius and far from one another in the phase portrait.

For fixed β, as γ is increased negatively, these limit cycles grow in size and thus approach one another, ultimately reaching sufficient proximity to form a 'channel' between them. As indicated in the inset to Figure 5(b), which shows a portion of a single trajectory traversing this channel, the motion zig-zags between the two limit cycles, in this case starting from the bottom (lower magnitudes) and exiting from the top. Once the trajectory leaves the channel the distance between successive points visited on the two limit cycles is much larger, giving rise to the higher amplitude oscilations observed in the time series. As γ is increased in magnitude, the limit cycles completely overlap leading to $u \simeq v$ while the trajectory is within the channel. Figure 6 displays a time series and phase portrait of such a case. Further increases in the magnitude of γ then lead to intertwining of the limit cycles and considerably more complex trajectories.

This type I *intermittency* is already present at $\beta=1.1$, and it persists in a range of γ depending on β all the way to the reverse bifurcations back to the single-frequency periodic state shown in Plates 1(a) and 2(a) for β between 3.2 and 3.3. It is interesting to note, however, that details of the temporal behaviour exhibited in the time series and phase portraits

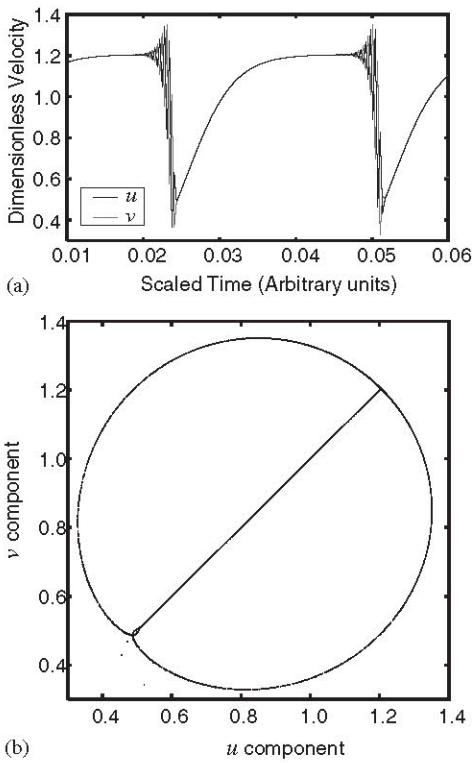

Figure 6. Description of Type I intermittency (cont.). $(\beta, \gamma) = (1.1, -1.017)$: (a) time series; (b) phase portrait.

change quite drastically as β is increased over this range while choosing γ so as to remain in the type I intermittency regime.

For low values of β, intermittency occurs well ahead of onset of broadband behaviour; the phase portraits of the corresponding attractors are relatively simple (as in Figure 6(b)), and mild SIC is observed only *after* complete overlap of the two quasiperiodic limit cycles. Moreover, true SIC is not observed. But as β is increased, the transition to broadband behaviour begins to occur for smaller (absolute) values of γ as the complexity of behaviour increases *within* each of the limit cycles. This is first recognized by a slight broadening of the point set covered by the limit cycles in a manner reminiscent of effects of 'self similarity' in the Hénon attractor (see, e.g. Figures 3–6 in Reference [23]). Figure 7 provides a typical time series and phase portrait with inset corresponding to $\beta = 2.5$ and $\gamma = -0.7$, showing early stages of this effect. Notice that the limit cycles have not yet overlapped; but they are in close proximity, and mild 'channelling' effects are evident in Figure 7(a). The power spectrum for this case (Figure 2(c)) is seen to be noisy quasiperiodic (w/fundamental), as might be expected from the self-similar broadening of trajectories seen in Figure 7(b).

Further increases in β result in far more irregular behaviour of trajectories and corresponding complexity of phase portaits as indicated in Figure 8. This case was computed with $(\beta, \gamma) = (2.8, -0.54)$ and exhibits a noisy quasiperiodic psd. The two limit cycles are

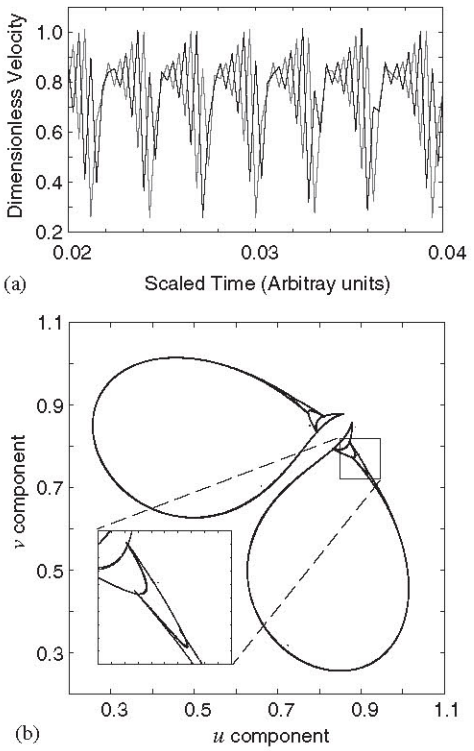

Figure 7. Attractor development with increasing β; $(\beta, \gamma) = (2.5, -0.7)$. (a) time series for u and v velocity components; (b) phase portrait.

relatively far apart with only very limited channelling effects apparent in the time series. But it is clear that behaviour has already become quite complex *within* each of these.

Of the three types of intermittency discussed in Reference [33], types I and III appear to be more wide spread (only these can occur in 1-D). We have identified what appears to be *type* III *intermittency* in the time series produced by Equations (14), but we have not checked behaviour of Floquet exponents to confirm this. This type of behaviour is characterized by fairly long segments of regular periodic oscillations occasionally interrupted by chaotic bursts with amplitudes greater than those of the periodic intervals. As the bifurcation parameter is increased, the frequency of these 'turbulent' episodes increases, and ultimately this bursting behaviour is dominant with only infrequent 'relaminarization' to periodicity.

Figure 9 displays an example of type III intermittency. Parts (a) and (b) of this figure display time series of the two velocity components, while part (c) contains the phase portrait. These were computed with $\beta = 3.8$, and $\gamma = 0.45$. A check of Plate 2(b) shows that this corresponds to the region immediately above the high-β periodic regime. As we have already indicated, intermittency cannot be determined from the power spectrum, and moreover, classification in the context of the algorithm we are employing is somewhat ambivalent in this particular case simply because the behaviour is, in a sense, non-stationary: it transitions between periodic and chaotic at unpredictable times, and for equally unpredictable durations.

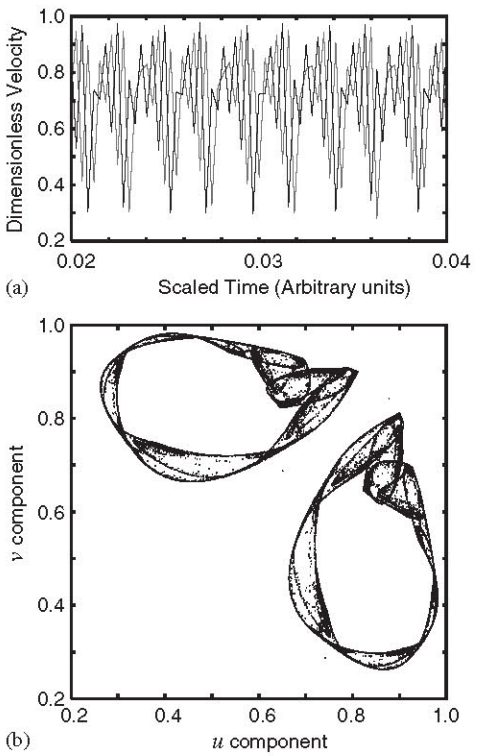

Figure 8. Attractor development with increasing β (cont.); $(\beta,\gamma)=(2.8,-0.54)$. (a) time series for u and v velocity components; (b) phase portrait.

The regime map indicates noisy quasiperiodicity for this behaviour, but the frequencies corresponding to this are difficult to detect in the psds. At the same time, as we will show below, although the power spectrum shows broadband behaviour, the auto correlation has only minimal decay due to retention of a strong component at the fundamental frequency.

The time series in Figures 9(a) and (b) indicate very strong cross-correlation of the velocity components in the sense that turbulent bursts occur simultaneously in the two components, although the bursts differ in detail between u and v. In particular, moderate-amplitude (measured peak to peak) bursts resulting from relatively slow growth in amplitude in one component are accompanied by high-amplitude bursts whose onset follows decreasing amplitude oscillations in the other component. The lower amplitudes occurring during periodic intervals are the result of trajectories zig-zagging between the two curves highlighted in the phase portrait in a manner analogous to what occurs between limit cycles in type 1 intermittency. Existence of such curves within the attractor appears to be a characteristic feature of type III intermittency in this 2-D discrete case.

Equations (14) are capable of producing at least an additional type of intermittency; it is not clear that this is of the type II discussed in Reference [33], but this is not ruled out by theory. It contains aspects of both types I and III, and we display it here in Figure 10 in terms of a u-component time series corresponding to $\beta=3.69$, and $\gamma=0.45$. Results from both

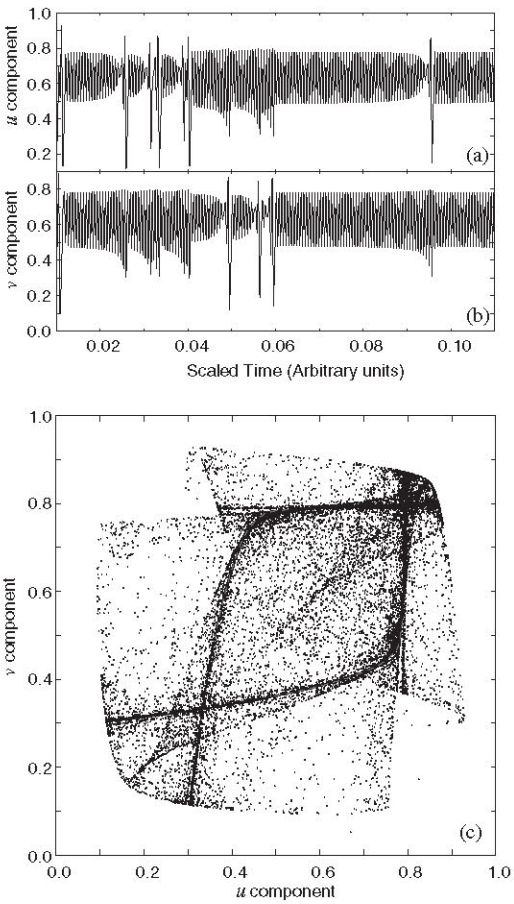

Figure 9. Type III intermittency; $(\beta,\gamma)=(3.8,0.45)$. (a) u-component time series; (b) v-component time series; (c) phase portrait.

initial conditions are displayed (the standard one in black) to emphasize the SIC property. Of particular interest in this case is that SIC, itself, appears to be somewhat 'intermittent.' Notice that in the interval $(\sim 0.074, \sim 0.079)$ the two different solutions are identical to within plotting accuracy, after which they rapidly separate. Such intervals occur repeatedly, and at unpredictable times, throughout the time series.

We conclude this section on time series with some interesting specific cases. The first of these is one in which u and v are perfectly correlated; i.e. $\overline{uv}=1.0$, but the behaviour is chaotic *and* SIC. This is shown in Figure 11, with parts (a) and (b) displaying the two separate velocity component time series and part (c) showing the u component for both the 'standard' and 'alternative' initial conditions employed throughout this study. The phase portrait is uninteresting in this case; as one should expect, it is merely a straight line at a 45° angle, and we do not present it.

The second case of interest is associated with further discussion of the apparently periodic time series displayed in Figure 3(k) which has a corresponding noisy power spectrum (see

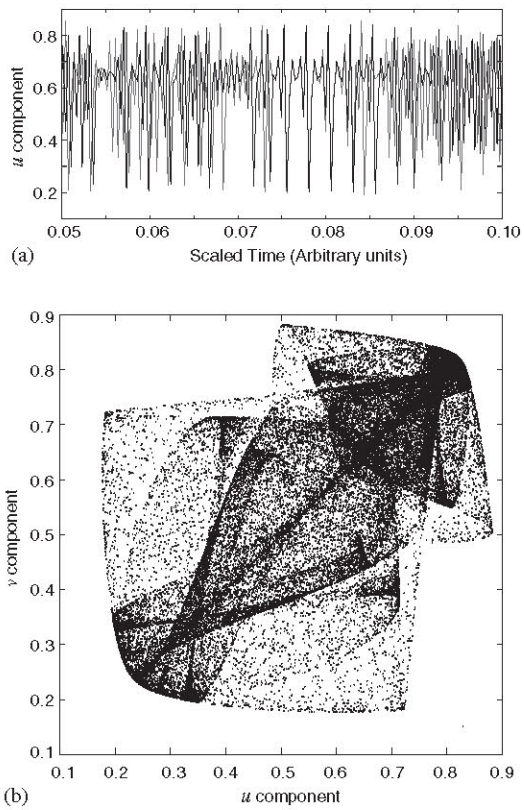

Figure 10. Intermittency $(\beta, \gamma) = (3.69, 0.45)$: (a) u-component time series for two different initial conditions; and (b) phase portrait.

Figure 2(f)). The resolution of this inconsistency can be deduced from Figure 12 which presents a very long segment of the time series for this case: $\beta = 3.83, \gamma = -0.0678$. Part (a) of the figure corresponds to our standard initial conditions, and part (b) shows results for the alternative conditions. Both figures indicate significant intervals of periodic behaviour (much more so in part (a)) that are much longer than the time interval captured in Figure 3(k). These are cases of type III intermittency; they are obviously extremely SIC in general despite having long subintervals of very regular, non-chaotic behaviour.

We close this discussion of time series with a final figure providing a direct comparison of the qualitative features of behaviour in five different regions of the regime maps Plates 1–3, all corresponding to broadband power spectra w/o fundamental. Because one would expect this to most closely represent, fully developed turbulence, it is of interest to examine these states in some detail. Figure 13 displays the pertinent results. Although all parts of this figure show similarities with regard to peak-to-peak amplitudes of fluctuations and general chaotic appearance, close examination reveals that each differs from the others in detail. All of the figures show at least some evidence of type I intermittency, but this is very minimal in part (c) which seems to best approximate fully developed turbulence. This was computed

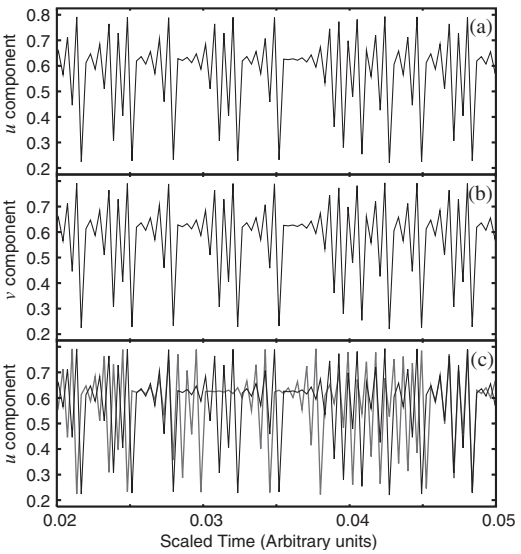

Figure 11. Extremely SIC, but with perfect cross correlation; $(\beta, \gamma) = (3.7, 0.6166)$: (a) u-component time series; (b) v-component time series; and (c) u-component time series for two different initial conditions.

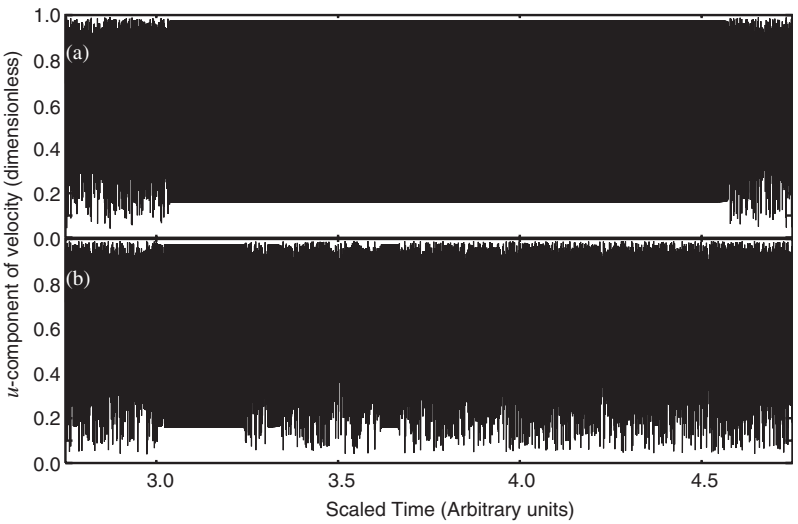

Figure 12. Long time series of type III intermittency; $(\beta = 3.83, \gamma = -0.0678)$: (a) standard initial conditions; and (b) alternative conditions.

with $\beta = 3.9, \gamma = -0.03$, corresponding to the far lower right-hand portions of the yellow regions in Plates 1(a) and 2(b). Type I intermittency appears to be most prevalent in part (a) corresponding to $\beta = 2.9, \gamma = -0.55$, in the low-$\beta$ chaotic region occurring prior to the reverse bifurcations back to periodicity. But significant type I intermittency also appears in the time

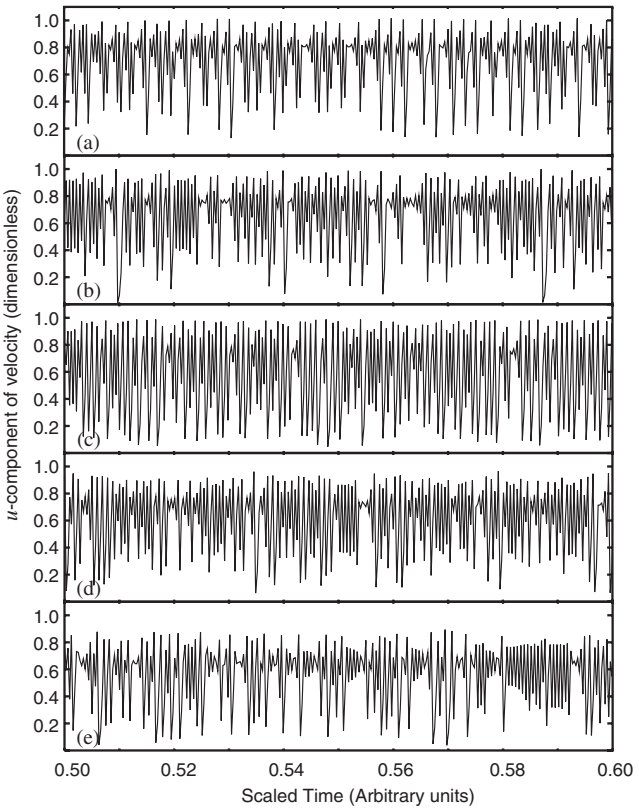

Figure 13. Comparison of time series with broadband power spectra: (a) $\beta = 2.9, \gamma = -0.55$; (b) $\beta = 3.7, \gamma = -0.15$; (c) $\beta = 3.9, \gamma = -0.03$; (d) $\beta = 3.9, \gamma = 0.15$; and (e) $\beta = 3.87, \gamma = 0.55$.

series of part (b), computed with $\beta = 3.7, \gamma = -0.15$. This is in the region preceding another reverse bifurcation, but in this case one that leads to periodicity with a lower fundamental frequency. Both parts (d) and (e) show small segments of type I intermittency, and quite pronounced type III intermittency, especially in part (e). Both of these correspond to high β and $\gamma > 0 : \beta = 3.9, \gamma = 0.15$, and $\beta = 3.87, \gamma = 0.55$, respectively.

It is important to note that the power spectra are very similar for all of these time series—broadband w/o fundamental, and yet details of appearance of the time series are quite different. This demonstrates that in the context of fitting experimental data, as in References [10, 11], use of the psd is not sufficient because different time series can lead to (essentially) the same psd. Moreover, in this same vein, it is clear from these examples that the psd does not readily quantify intermittency; it is the type and degree of intermittency that seem to distinguish these time series.

3.4. Correlations, skewness and flatness

In this section we present some properties of the solutions to Equations (14) that are widely used in studies of physical turbulence. Our motivation for this is to provide an initial link

between these equations and behaviours of actual N–S flows. In particular, these statistical quantities have been extensively studied, and much is known regarding their observed values. In addition, we will see that in some cases one, or more, of these quantities can aid in providing unambiguous classification of behaviour in cases (noted above) for which this was not possible with a psd alone. On the other hand, it will also be evident that in most cases the psd, in conjunction with our classification scheme, will provide a more reliable identification of behaviour type. We will begin with discussions of autocorrelation and cross correlation in the first subsection, and follow this with a subsection on skewness and flatness.

3.4.1. Auto- and cross-correlations. Autocorrelation provides a means of determining how long a time series 'remembers where it has been.' For a discrete time series as we deal with here, say $\{a^{(n)}\}_{n=1}^{N}$, we calculate the autocorrelation as a function of the correlation time interval $m\Delta t,\ m = 1, 2, \ldots, m_{\max} \ll N$:

$$C(m) \equiv \frac{1/(N-m-1)\sum_{n=1}^{N-m}(a^{n+m}-\bar{a})(a^{n}-\bar{a})}{1/(N-1)\sum_{n=1}^{N}(a^{n}-\bar{a})^2} \simeq \frac{\langle u'(t), u'(t+m\Delta t)\rangle}{\|u'^2\|_2^2} \tag{15}$$

Here $u' \equiv u - \bar{u}$, with overbar denoting a time average; $\langle \cdot, \cdot \rangle$ is the usual inner product, and $\|\cdot\|_2$ is the L^2 norm with respect to time. That is, we compute autocorrelations of the fluctuating part of $\{a^{(n)}\}$ which has been sampled with a discrete interval Δt. Clearly, from Equation (15) it can be seen that $-1 \leqslant C(m) \leqslant 1$. Furthermore, periodic and quasiperiodic functions have corresponding autocorrelations.

Of more interest are the autocorrelations of the noisy states discussed above in terms of their psds and time series, because for these the behaviour is sometimes counter intuitive. In the following figures we present results for autocorrelations with $m_{\max} = 750$. (Recall that $N = 10^4$ for calculation of statistics, and that the time series have been computed for 5×10^4 steps.) This value of $m_{\max}$ is easily sufficient to allow one to recognize all important trends. Figure 14 provides autocorrelations for each of the noisy cases for which we have presented psds in Figure 2.

In discussing this figure, we first note that the maximum computed correlation time was 0.24 in the *same* arbitrary units employed for the time series. We have displayed only the first 0.1 units because the trends do not change in the remaining interval, and the plots are more easily read and interpreted over this shorter time. From part (a) of the figure (noisy subharmonic, corresponding to the psd of Figure 2(a)) we see that despite the broadband noise shown in Figure 2(a), the fundamental and subharmonic frequencies dominate the behaviour. There is no discernable decay of autocorrelation, which is consistent with our earlier observation that the noise is at very low power compared with the harmonic peaks, and that the time series (Figure 3(f)) shows only slight deviations from noise-free subharmonic behaviour. Part (b) of Figure 14 presents noisy phase-locked behaviour corresponding to the psd of Figure 2(b) and the time series in Figure 3(g). As with the previous case, there is no obvious decay of the autocorrelation, and the reasons for this are similar to those for part (a).

The more interesting cases begin with part (c), which is noisy quasiperiodic w/fundamental. Here we see a distinct, but very slow, decay of the correlation function, providing a significant difference between this and the noisy phase-locked case. A comparison of the psds for these two cases in Figure 2 provides a hint that in some situations these two behaviours would be

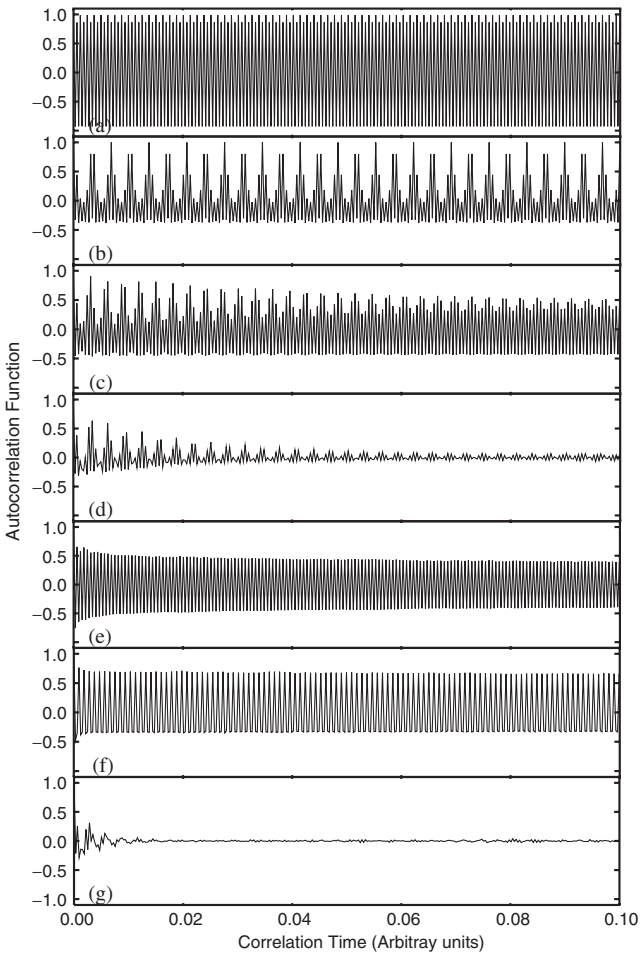

Figure 14. Autocorrelations corresponding to power spectra of Figure 2: (a) subharmonic; (b) phase locked; (c) quasiperiodic w/fundamental; (d) quasiperiodic w/o fundamental; (e) broadband w/fundamental; (f) broadband w/different fundamental; and (g) broadband w/o fundamental.

very difficult to distinguish from the psd alone, and decay of the autocorrelation may yield a means for unequivocally separating these two behaviours.

We have earlier remarked that existence of the fundamental frequency in the power spectrum appears to be a determining factor in whether or not the autocorrelation decays rapidly. The final four parts of this figure display this. Part (d) is the noisy quasiperiodicity whose psd is presented in Figure 2(d). There is no fundamental frequency, and we see fairly rapid decay of the autocorrelation. But it is of interest to note that the autocorrelation function retains a distinct regularity, even at rather low values. In contrast to this rather rapid decay is the quite slow decay shown in Figures 14(e) and (f). These correspond to completely broadband spectra, but with a fundamental still present. We have earlier noted that such cases would be difficult to distinguish from noisy periodic, and these autocorrelations substantiate this.

The final case in Figure 14 corresponds to a broadband power spectrum w/o fundamental. Here we see that the autocorrelation rapidly decays to essentially zero with the oscillations about zero showing no regular pattern, in contrast to the noisy quasiperiodic w/o fundamental case. Thus, again, the autocorrelation may provide a means of separating these two cases in borderline situations where the power spectra show some remnants of quasiperiodicity but are mainly broadband.

Cross correlations are among the more valuable statistical quantities associated with a turbulent flow field simply because, up to rescaling, these are the off-diagonal terms of the Reynolds stress tensor. In the context of RANS second-order closures, modelling the PDEs whose solutions are these cross correlations is crucial. Moreover, less than satisfactory accuracy of these quantities as computed in LES is one of the main shortcomings of this form of turbulence modelling. In the case of the discrete data considered here, we calculate the cross-correlation as

$$\overline{u'v'} \simeq \frac{\sum_{n=1}^{N}(a^{(n)}-\bar{a})(b^{(n)}-\bar{b})}{\frac{1}{2}\left[\sum_{n=1}^{N}(a^{(n)}-\bar{a})^2+(b^{(n)}-\bar{b})^2\right]} \tag{16}$$

Plate 4 displays the $\overline{u'v'}$ cross correlations obtained from Equations (14) in computer runs described earlier; they are computed and output simultaneously with the spectral characterizations already discussed. There are several important features to observe in this figure. First, very light green regions correspond to nearly zero correlation of either sign, and comparisons of Plate 4 and either Plate 1(a) or 2(b) shows that these regions generally coincide with a broadband spectrum w/o the fundamental frequency. On the other hand, it is also clear from these figures that the regions of broadband psds are considerably more extensive than are those of nearly zero cross correlation. We next observe that the regions of positive $\overline{u'v'}$ correlation are in the part of the colour table going toward red, and it can be seen that all of the steady, and much of the periodic, regions of the regime map exhibit these colors for their cross correlations. Furthermore, all high-β, high-γ regimes show positive cross-correlation except those in the high-β periodic regime. It is also interesting to observe that no distinction between phase lock and quasiperiodicity can be detected in the cross correlations; but they do correctly indicate subharmonic and periodic with a different fundamental frequency, just as does the spectral analysis.

Colours ranging from dark green through various shades of blue correspond to negative $\overline{u'v'}$ correlations. We first note that essentially all low-β behaviour beginning with the transition to periodicity in the Ruelle and Takens sequence possess this character. In addition, as already mentioned, the high-β periodic region as well as the bridge connecting it to the low-β regimes show negative cross correlations. It is also interesting to note from Plate 4 that both subharmonic and periodic regimes undergo two sign changes ($+\rightarrow-\rightarrow+$) of their correlations for β fixed and γ varied over the interval in which bounded behaviours occur. This aspect cannot be detected with the psd.

Finally, we focus on the inset to Plate 4. The main purpose of this inset is to again emphasize the apparently fractal nature of the $\beta-\gamma$ basins of attraction for Equations (14), and to demonstrate the richness of behaviours that can occur in very small subsets of the $\beta-\gamma$ domain. The inset shows cross correlations in a neighbourhood of the lower left-hand corner of the high-β region of single-frequency periodicity. On the left side of this figure we see highly (positively) correlated subharmonic and quasiperiodic states, as well as those associated

with a broadband spectrum *with fundamental*. As we move towards the centre of the figure, we see a sharp transition to negative (and still very high) correlations in, and near the bottom of, the high-β periodic region. But below this region there is no sharp transition, and the boundary between positive and negative correlations is probably fractal. We also see vertical streaks of positive correlation in regions of β corresponding to the 'windows of periodicity' in the 1-D logistic map, as detected in the spectral analysis as well.

3.4.2. Skewness and flatness. We next consider skewness of the derivatives of Equations (14). It is known (see, e.g. Reference [7]) that skewness of spatial derivatives in a turbulent flow are typically in the range $(-0.6, -0.3)$ with values outside this range occasionally observed. In the case of Equations (14) we can only obtain discrete time derivatives (which might be transformed to spatial derivatives by invoking Taylor's hypothesis), but it is easily checked from Equations (5) that if $\|u\|$ and $\|v\|$ are $\mathcal{O}(1)$, then the time derivative is of the same order of magnitude as are the spatial derivatives for large Re. Thus, for the present purposes we define a dimensionless skewness of the (discrete) time derivative as

$$S = \frac{\overline{(\Delta u/\Delta t)^3}}{(\overline{(\Delta u/\Delta t)^2})^{3/2}} \simeq \frac{1/(N-1)\sum_{n=1}^{N}(a^{(n)} - a^{(n-1)})^3}{\left[1/(N-1)\sum_{n=1}^{N}(a^{(n)} - a^{(n-1)})^2\right]^{3/2}} \tag{17}$$

We see from (17) that S is independent of the time scale, so our use of arbitrary time increments will have no influence on the computed value of S.

In Plate 5 we display the contours of skewness as a function of β and γ as we have done with the cross-correlation. We observe that the range of computed values is generally similar to experimental observations, although we must view this with some caution in light of differences in detail between temporal and spatial derivatives. It can be seen from this figure that the skewness values corresponding to most of the chaotic portion of the regime maps, Plates 1(a) and 2, are generally between -0.9 and -0.1, but with a region of significant size in the low-β, high-$|\gamma|$ regime where $S < -1.0$. In particular, it appears that the regions of the regime map that one would expect to utilize most often in a turbulence model exhibit values of skewness that are consistent, in a general sense, with experimental observations.

Contours of flatness are displayed in Plate 6. In this case we have used flatness of the u component of velocity, computed as follows:

$$F \equiv \frac{\overline{u'^4}}{(\overline{u'^2})^2} \simeq \frac{1/(N-1)\sum_{n=1}^{N}(a^{(n)} - \bar{a})^4}{\left[1/(N-1)\sum_{n=1}^{N}(a^{(n)} - \bar{a})^2\right]^2} \tag{18}$$

The figure indicates that values of flatness are generally below the value corresponding to a Gaussian probability density, $F = 3$. From Tennekes and Lumley [34] and Frisch [7] we know that $F < 3$ corresponds to a probability density function (pdf) with smaller variance than Gaussian, and conversely, the pdf for $F > 3$ will display greater than Gaussian variance. We have also noted above that flatness can be related to the small-scale intermittency, with high values of flatness corresponding to a highly-intermittent signal. The results displayed in Plate 6 are consistent with this in only a general way. In particular, recall that the low-β, high-$|\gamma|$ with $\gamma < 0$ results show very strong type I intermittency, and this region in Plate 6 indicates values of flatness both greater than three and less than three. Furthermore, regions of type III intermittency generally show values of flatness less than three.

These observations seem to imply that the results from Equations (14) are not as intermittent as is physical high-Re turbulence; the maximum value of flatness found in the calculations was only slightly greater than five, whereas experimentally observed values are sometimes as much as twice this value, and occasionally even more. Nevertheless, the general trends seem to be correct. We noted above in Section 2 that γ is directly proportional to the wavenumber $\mathbf{k}$ (actually a component of the wave vector, k), and the degree of intermittency is observed to increase on small scales, i.e. at high values of $|\mathbf{k}|$. Plate 6 shows generally high values of F at the lowest (high-amplitude, negative) values of γ, which is consistent with this.

Furthermore, it is possible to increase the level of intermittency by employing linear combinations of any particular DDS as described in Reference [16]. Indeed, we have found that linear combinations of the logistic map (1) are capable of fitting experimental data for backward-facing step-like flows (see McDonough and Yang [35] and Roclawski *et al.* [36]), when a single logistic map is not capable of this. In light of the fact that, by construction, Equations (14) model only a single wave number of the N–S equations solutions, it is reasonable to expect that more than a single realization might be needed to completely match properties of physical flows.

3.5. Further discussion

In this final subsection we will elaborate further on some of the discussions of the figures begun above, and in addition provide comments on advantages and disadvantages of the proposed modelling approach while comparing it to similar methods. We will then briefly indicate some details on how this information might be used in practice and, along with this, indicate the benefit of a close connection with laboratory experiments in attempting to explore the potential of such models.

We begin by noting the general similarities seen in the various contour plots for power spectral characterization, cross correlation, skewness and flatness. Each of these plots exhibits certain specific features of its own, but at the same time all are rather similar, indicating an overall consistency across the several representations as β and γ are varied. Comparison of Plates 1, 4, 5 and 6 shows that the power spectral analysis (Plate 1(a)) provides the best overall delineation of the various regimes, which is why we have placed considerable emphasis on this particular mode of characterization. At the same time, there are specific details highlighted by the cross correlations of Plate 4 that are not available in the power spectral analysis: namely, the manner in which sign changes occur in the fluctuating parts of the velocity components as the bifurcation parameters are varied, and hence, the signs of the Reynolds stresses. But neither skewness nor flatness seems capable of discriminating between the various types of chaotic behaviours described by the power spectral analysis. In addition, they do not even reliably distinguish the quasiperiodic and phase-locked regimes.

We next remind the reader that all of the results presented herein, with just a few already noted exceptions (especially Plate 3), have been computed with a single set of initial conditions. Obviously, there exists an uncountably infinite set of possible combinations of $a^{(0)}$ and $b^{(0)}$. A comparison of Plates 1(a) and 3 suggests that our standard choice has been the slightly more conservative of the two alternatives considered in the sense that it results in a smaller region of non-divergent combinations of β and γ. But at present we do not know whether this is the minimal region (it probably is not), and for purposes of constructing reliable models it will be necessary to stay well within the non-divergent region for all possible

initial conditions. Studies by Bible and McDonough [31] have partially addressed this issue, both for equal and nonequal βs and γs.

The assumption of equal βs and γs is itself an important area requiring further study. We noted at the outset that the choice $\beta_1 = \beta_2$ and $\gamma_1 = \gamma_2$ provided a natural way to limit the extent of these initial investigations, and at least the assumption of equal βs is not unreasonable. On the other hand, in some (possibly most!) physical flow situations the assumption of equal γs is probably not realistic. In our discussions of flatness, with computed values summarized in Plate 6, we have observed that our results are somewhat lower than those generally seen in physical measurements. In this regard we note that with $\gamma_1 = \gamma_2$ it must be the case that the flatness of u equals the flatness of v; i.e. $F(u) = F(v)$, and there is experimental and DNS evidence that this is not the case for small values of y^+, the inner-scale distance from a solid bounding surface. Origins of this discrepancy are discussed in detail in Xu *et al.* [37]. Recent work [22] has examined the effects of $\gamma_1 \neq \gamma_2$ as well as $\beta_1 \neq \beta_2$, to a lesser extent. Clearly, our interpretation of the physical connection of γ with a velocity gradient suggests that in most situations $\gamma_1 \neq \gamma_2$ is likely, and results reported in Reference [22] reflect this.

We mentioned in Section 2 that Equations (14) arise in a way that is at least similar to other models exhibiting chaotic behaviour. It is worthwhile at this point, with the generic behaviour of these equations in hand, to revisit this earlier discussion. In terms of the manner of derivation, the best-known similar system is probably the Lorenz model [24]. Although this is a differential system, after numerical discretization is applied the resulting algebraic equations are not extremely different from Equations (14). There are, however, two rather fundamental differences. The first is that the Lorenz equations comprise an autonomous system of three differential equations, the minimum needed for existence of chaotic solutions (see, e.g. Reference [33]); so the corresponding discretization consists of three algebraic equations, rather than the two equations of (14). Indeed, it is crucial to recognize that Equations (14) arose from the system of only two differential equations (8) (which, itself is incapable of producing chaos), and this implies that it is the transformation consisting of Equations (11,12) that has played a fundamental role in producing the observed turbulent-like behaviours.

The second major difference between the derivation of the Lorenz system and what we have done here is that in the former the Galerkin approximation was truncated after the lowest mode. This, of course, is not reasonable in the context of a subgrid-scale turbulence model, but we must bear in mind that SGS modelling was not the original goal in constructing the Lorenz equations. By way of contrast, Equations (14) are derived to represent a single *arbitrary* mode of a Fourier representation of a N–S equations solution, a viewpoint generally consistent with SGS modelling if we choose that mode (or, possibly several of them) corresponding to a high wavenumber.

It is also worth recalling that Equations (14) have some of the basic structure of the Hénon map [23], as we have earlier observed. But here, again, there are significant fundamental differences, some of which have been noted above. It was Hénon's intention to produce what might be viewed as a Poincaré map of the Lorenz equations, and as we might conclude from the preceding discussions, Equations (14) cannot be viewed as a Poincaré map of Equations (8).

The most important distinction between Equations (14) and other quadratic maps that have been widely studied, including that in Reference [23], is the nature of the coupling, and the resulting symmetry between the two equations of the system. The complete consequences of this are yet to be fully investigated, but retaining bilinearity in the coupling terms of both equations renders use of analytical methods of study much more difficult. All other

2-D quadratic systems studied in the past, of which the authors are aware, employed linear coupling in at least one equation. Even in such cases analysis is quite difficult unless additional constraints are imposed (e.g. area preservation), leading Lyubich [38] to note, 'Even for diffeomorphisms in dimension two this looks like a project for the whole twenty-first century.'

At this point it is reasonable to ask, 'Of what practical use is the 'poor man's N–S equation'?' Is it nothing more than a mathematical curiosity with no actual utility, or might it be capable of aiding prediction of flow behaviour? We have suggested from the start that our intention is to employ Equations (14) as part of a LES SGS modelling formalism introduced in [15] and described in detail in References [16, 17] (also see Sagaut [39]). Here, we will present no more than an outline of this approach since it has been thoroughly documented in Reference [17]. On the other hand, some description is needed to provide the framework into which results of Equations (14) would be cast.

The treatment of the numerical solution of the N–S equations given in References [15–17] differs from usual LES in three key, related ways: (i) the equations of motion are not filtered; (ii) subgrid-scale models are constructed for primitive variable fluctuations—not for their statistics, and (iii) SGS model results are directly added to the large-scale part of the solution. Clearly, the first item enables the second which, we contend, simplifies the SGS modelling task, at least in the sense that it facilitates closer connection to actual flow physics on the sub-grid scales. At the same time deleting application of the filter to the equations raises the question of how to define the resolved scales and, possibly even more important, how to avoid effects of aliasing in an under-resolved large-scale part of the solution. These issues have been addressed in the cited references, and in many respects are irrelevant for the present study in any case. But the preceding discussion does provide the motivation and setting for the current work.

The form of the SGS model proposed in the above references consists of modelling each velocity component (actually, the high-wave number contribution) as a product of three factors: (i) an amplitude factor constructed from Kolmogorov's theories as described in Reference [7], (ii) an anisotropy correction obtained by invoking a scale-similarity argument as is done in constructing typical dynamic subgrid-scale models (see Meneveau and Katz [40] for a recent review), and (iii) a discrete dynamical system to produce temporal fluctuations. It is worth noting that, in principle, the modelling procedure described in Reference [17] could be used to estimate SGS stresses in the context of Domaradzki's estimation method [12, 13], and it might also be used in place of the random number generators employed in the *linear-eddy* modelling approach of Kerstein and various co-workers (see, e.g. Kerstein [41]). In all such cases, a realistic map M would be desirable, but possibly not necessary in the linear-eddy model case.

In References [15, 16] and later simulations, e.g., McDonough *et al*. [42] the same 1-D DDS was used for each solution component, but with independent realizations of the map for each component. Clearly, this implies that some additional correlation procedure is needed (see References [16, 17]), but it also implies that fluctuations of all components behave in the same way. This latter property led to inaccurate heat transfer predictions in Reference [42], and the review by Warhaft [43] indicates that the structure of passive scalar fluctuations is not the same as that of the fluctuating flow field advecting them. This motivated the present authors to introduce a completely coupled DDS in the context of reduced-kinetics H_2–O_2 combustion in Reference [44]; the current study provides a far more detailed analysis of the flow field alone.

What is clear from discussions in References [15–17, 42] is that the bifurcation parameter(s) of each realization of the DDS(s) must be set locally (in space and time) based on the resolved-scale flow field and its gradients. This, itself, constitutes a mapping, say $\mathscr{M}:(u,v,\nabla u,\nabla v)\rightarrow(\beta_1,\beta_2,\gamma_1,\gamma_2)$, and the details of this mapping are, *a priori*, unknown. In the cited references we employed (a slight modification of) the 1-D logistic map (1) as our DDS, so there was only a single bifurcation parameter. In this case it was not difficult to construct an *ad hoc* mapping, but it is not clear that it always accomplished what was intended. The present situation is for more complex, necessitating the detailed study of the DDS structure we have presented herein, and relating this to physically-measurable quantities such as $\overline{u'v'}$, $S(\mathrm{d}u/\mathrm{d}t)$ and $F(u')$. It should also be noted, in addition, that it has recently been demonstrated (McDonough [45] and McDonough and Holloway [46]) that a two-factor model of the type alluded to above containing three factors provides a simpler approach, and that the amplitude of such a formalism can be constructed from high-pass filtered resolved-scale LES results using local (in space) power-law scalings related-to second-order structure functions, *a la* the Kolmogorov (K62) theory as described in Reference [7]. The poor man's Navier–Stokes equations we have analysed herein provide a natural fluctuating component for this form of model.

We also point out that Equations (14) have another potential application, namely, real-time control. It has been shown in Reference [47] that DDSs can successfully model the complete velocity behaviour as well as the high-pass filtered part. In fact, it was only the former that was originally treated in References [10, 11]. This implies that if it is known, *a priori*, what range of flow behaviours a controller must respond to (and this is usually the case), then the poor man's N–S equations, with the help of experimental data, can be used to design and implement controllers for fluid flows.

4. SUMMARY AND CONCLUSIONS

In this paper we have derived a new discrete dynamical system directly from the 2-D N–S equations, and we have provided detailed numerical characterization of the possible behaviours for the restricted case corresponding to setting the four bifurcation parameters equal in pairs. We have reported results summarized in the form of regime maps for over 10^7 individual cases and have shown that although the DDS is extremely simple (and consequently very inexpensive to compute), it is capable of reproducing essentially all of the known behaviours of the N–S equations.

We conclude from these analyses, especially the realistic behaviours embodied in cross correlations, skewness and flatness, that the poor man's N–S equation has significant potential for building subgrid-scale models in the context of synthetic velocity forms of LES, but that this may require considerable effort to construct the necessary mappings from physical experimental data. Finally, we propose that such DDSs may prove valuable as real-time controllers of fluid flow phenomena because they appear to preserve the qualitative features of N–S flows and at the same time are very inexpensive to compute.

ACKNOWLEDGEMENTS

The authors wish to express their gratitude to the U.S. Air Force Office of Scientific Research (Grant # F49620-00-1-0258) and to NASA/EPSCoR (Grant # WKU 522653-00-10) for support of the research

reported here. In addition, the second author received assistance from the University of Kentucky Centre for Computational Sciences. This and access to computational facilities provided by the University of Kentucky Computing Center are gratefully acknowledged.

REFERENCES

1. May RM. Simple mathematical models with very complicated dynamics. *Nature* 1976; **261**:459–467.
2. Collet P, Eckmann J-P. *Iterated Maps of the Interval as Dynamical Systems*. Birkhäuser: Boston, 1980.
3. Lauwerier HA. One-dimensional iterative maps. In *Chaos*, Holden (ed.). Princeton University Press: Princeton, NJ, 1986; 39–57.
4. Alligood KT, Sauer TD, Yorke JA. *CHAOS An Introduction to Dynamical Systems*. Springer-Verlag: New York, 1997.
5. Feigenbaum MJ. Quantitative universality for a class of nonlinear transformations. *Journal of Statistical Physics* 1978; **19**:25–52.
6. Pulliam TH, Vastano JA. Transition to turbulence in an open unforced 2D flow. *Journal of Computational Physics* 1993; **105**:133–149.
7. Frisch U. *Turbulence The Legacy of A.N. Kolmogorov*. Cambridge University Press, Cambridge, 1995.
8. Abraham RH, Gardini L, Mira C. *Chaos in Discrete Dynamical Systems*. Springer-Verlag: New York, 1997.
9. Gollub JP, Benson SV. Many routes to turbulent convection. *Journal of Fluid Mechanics* 1980; **100**:449–470.
10. McDonough JM, Mukerji S, Chung S. A data-fitting procedure for chaotic time series. *Applied Mathematics and Computation* 1998; **95**:219–243.
11. Mukerji S, McDonough JM, Mengüç MP, Manivackasagam S, Chung S. Chaotic map models of soot fluctuations in turbulent diffusion flames. *International Journal of Heat and Mass Transfer* 1998; **41**:4095–4112.
12. Domaradzki JA, Saiki EM. A subgrid-scale model based on the estimation of unresolved scales of turbulence. *Physics of Fluids* 1997; **9**:2148–2164.
13. Kimmel SJ, Domaradzki JA. Large eddy simulations of Rayleigh–Bénard convection using subgrid scale estimation model. *Physics of Fluids* 2000; **12**:169–184.
14. Scotti A, Meneveau C. A fractal model for large eddy simulation of turbulent flow. *Physica D* 1999; **127**:198–232.
15. McDonough JM, Yang Y, Hylin EC. Modeling time-dependent turbulent flow over a backward-facing step via additive turbulent decomposition and chaotic maps. In *Proceedings of First Asian Computational Fluid Dynamics Conference*, Hui K, Chasnov (eds). Hong Kong University of Science and Technology: Hong Kong, 1995; 747–752.
16. Hylin EC. A Stochastic Model for small-scale turbulence. *PhD dissertation*, University of Kentucky, Department of Mechanical Engineering, 1997.
17. Hylin EC, McDonough JM. Chaotic small-scale velocity fields as prospective models for unresolved turbulence in an additive decomposition of the Navier–Stokes equations. *International Journal of Fluid Mechanics Research* 1999; **26**:539–567.
18. Dubois T, Jauberteau F, Temam R. *Dynamic Multilevel Methods and the Numerical Simulation of Turbulence*. Cambridge Univ. Press: Cambridge, 1999.
19. Constlantin P, Foias C. *Navier–Stokes Equations*. University of Chicago Press: Chicago, 1988.
20. Gresho PM. On the theory of semi-implicit projection methods for viscous incompressible flow and its implementation via a finite element method that also introduces a nearly consistent mass matrix. Part 1: theory. *International Journal for Numerical Methods in Fluids* 1990; **11**:587–620.
21. Bohr T, Jensen MH, Paladin G, Vulpiani A. *Dynamical Systems Approach to Turbulence*. Cambridge Univ. Press: Cambridge, 1998.
22. McDonough JM, Bible SA, Scoville J. Response to strain rate in a discrete dynamical model of the high-wavenumber Navier–Stokes equation. *Journal of Turbulence* 2004; in press.
23. Hénon M. A two-dimensional mapping with a strange attractor. *Communications in Mathematical Physics* 1976; **50**:69–77.
24. Lorenz EN. Deterministic nonperiodic flow. *Journal of the Atmospheric Sciences* 1963; **20**:130–141.
25. Yorke JA, Yorke ED. Chaotic behaviour and fluid dynamics. In *Hydrodynamic Instabilities and the Transition to Turbulence*, Swinney, Gollub (eds). Springer-Verlag: Berlin, 1981; 77–84.
26. Hénon M, Pomeau Y. Two strange attractors with a simple structure. In *Turbulence and the Navier–Stokes Equations*, Temam (ed), Lecture Notes in Mathematics, vol. 565. Springer-Verlag: Berlin, 1976; 29–68.
27. Frøyland J. *Introduction to Chaos and Coherences*. IOP Publishing, Ltd.: Bristol, 1992.
28. McDonough JM, Bywater RJ, Large-scale effects on local small-scale chaotic solutions to Burgers' equation. *A1AA Journal* 1986; **24**:1924–1930.
29. Grassberger P, Procaccia I. Characterization of strange attractors. *Physical Review Letters* 1983; **50**:346–349.

30. Wolfe A, Swift JB, Swinney HL, Vastano JA. Determining Lyapunov exponents from a time series. *Physica D* 1985; **16**:285–317.
31. Bible SA, McDonough JM. Basin of attraction of the two-dimensional 'poor man's Navier–Stokes equation'. *International Journal of Bifurcation and Chaos* 2003, accepted.
32. Ruelle D, Takens F. On the nature of turbulence. *Communications in Mathematical Physics* 1971; **20**:167–192.
33. Bergé P, Pomeau Y, Vidal C. *Order Within Chaos*. Wiley: New York, 1984.
34. Tennekes H, Lumley JL. *A First Course in Turbulence*. MIT Press: Cambridge, MA, 1972.
35. McDonough JM, Yang T. Parallelization of a chaotic dynamical systems analysis procedure. In *Parallel Computational Fluid Dynamics Practice and Theory*, Wilder *et al*. (eds). North-Holland Elsevier, Amsterdam, 2002; 253–260.
36. Roclawski H, Jacob JD, Yang T, McDonough JM. Experimental and Computational Investigation of Flow in Gas Turbine Passages. AIAA-2001-2925, Presented at 31*st AIAA Fluid Dynamics Conference and Exhibit*, Anaheim, CA, June 11–14, 2001.
37. Xu C, Zhang Z, den Toonder JMJ, Nieuwstadt FTM. Origin of high kurtosis in the viscous sublayer. Direct numerical simulation and experiment. *Physics of Fluids* 1996; **8**:1938–1944.
38. Lyubich M. The quadratic family as a qualitatively solvable model of chaos. *Notices*, *American Mathematical Society* 2000; **47**:1042–1052.
39. Sagaut P. *Large Eddy Simulation for Incompressible Flows*. Springer-Verlag: Berlin, 2001.
40. Meneveau C, Katz J. Scale-invariance and turbulence models for large-eddy simulations. *Annual Reviews of Fluid Mechanics* 2000; **32**:1–32.
41. Kerstein AR. A linear-eddy model of turbulent scalar transport and mixing. *Combustion Science and Technology* 1988; **60**:391–421.
42. McDonough JM, Garzón VB, Schulte DE. Effect of film-cooling hole location on turbulator heat transfer enhancement in turbine blade internal air-cooling circuits. ASME Paper 99-GT-141 presented at *ASME TURBO EXPO* 99, Indianapolis, IN, June 7–10, 1999.
43. Warhaft Z. Passive scalars in turbulent flows. *Annual Reviews of Fluid Mechanics* 2000; **32**:203–240.
44. McDonough JM, Huang MT. A low-dimensional model of turbulence—chemical kinetics interactions. Paper ISSM3-E8 in *Proceedings of Third International Symposium on Scale Modeling*, Nagoya, Japan, September 10–13, 2000.
45. McDonough JM. A 'synthetic scalar' subgrid-scale model for large-eddy simulation of turbulent combustion. Paper c34 in *Proceedings of* 2002 *Spring Technical Meeting Central States Section*, *The Combustion Institute*, Knoxville, TN, April 7–9, 2002.
46. McDonough JM, Holloway JC. An alternative approach to subgrid-scale modelling for les of turbulent combustion. Paper E33 in *Proceedings of the Third Joint Meeting of the US Sections of the Combustion Institute*, Chicago, IL, March 16–19, 2003.
47. Yang T, McDonough JM, Jacob JD. Poor man's Navier–Stokes equation model of turbulent flow. *AIAA Journal* 2003; **41**:1690–1696.

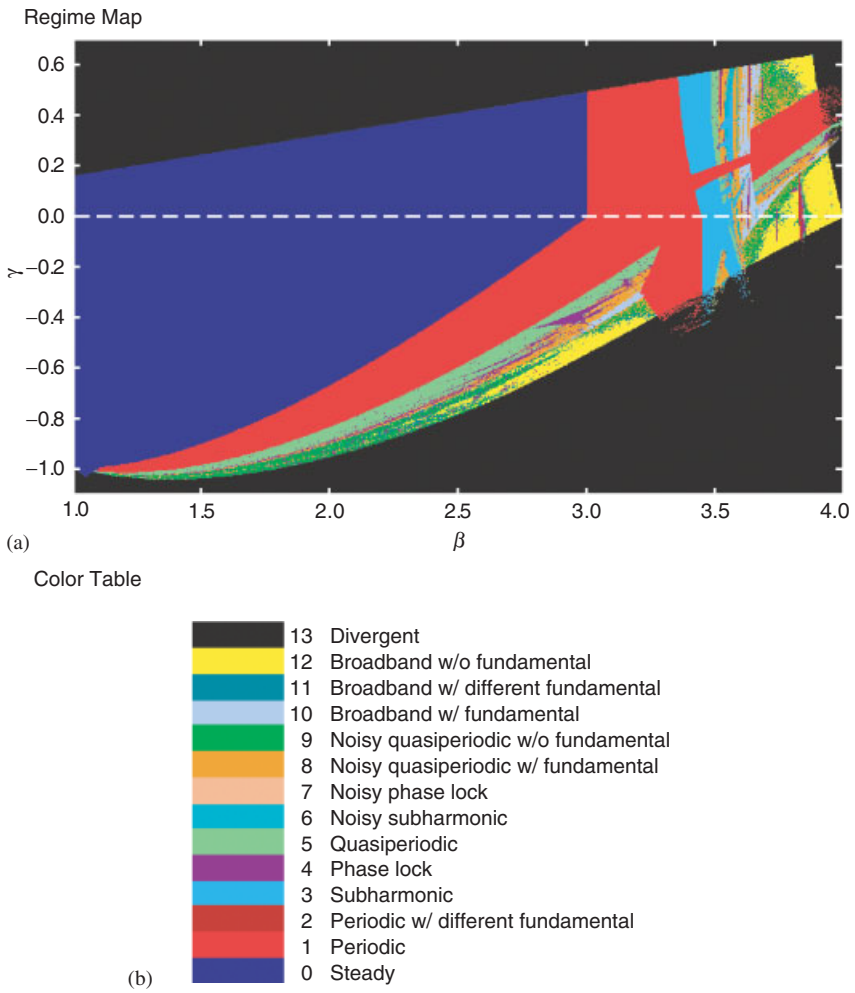

Plate 1. Regime Map: (a) regime map for entire domain of interest; and (b) colour table.

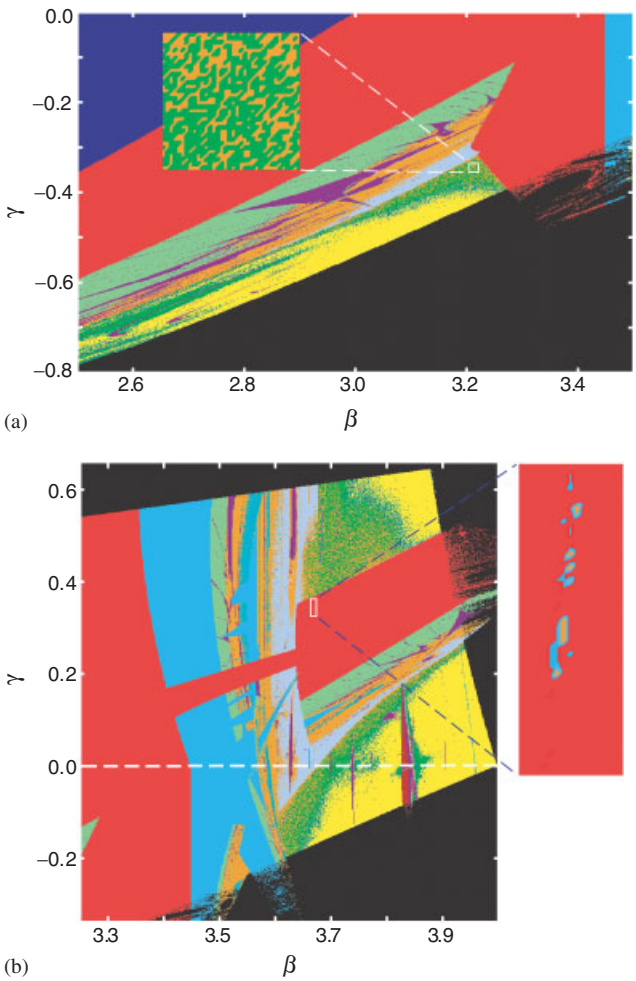

Plate 2. Regime map zoom-ins: (a) $(\beta, \gamma) \in [2.5, 3.5] \times [-0.8, 0.0]$; and (b) $(\beta, \gamma) \in [2.5, 3.5] \times [-0.8, 0.0]$.

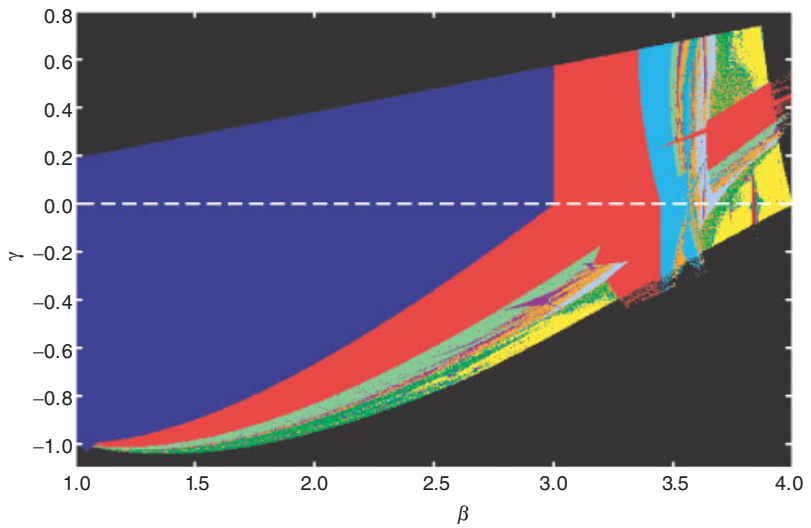

Plate 3. Regime map for different initial conditions.

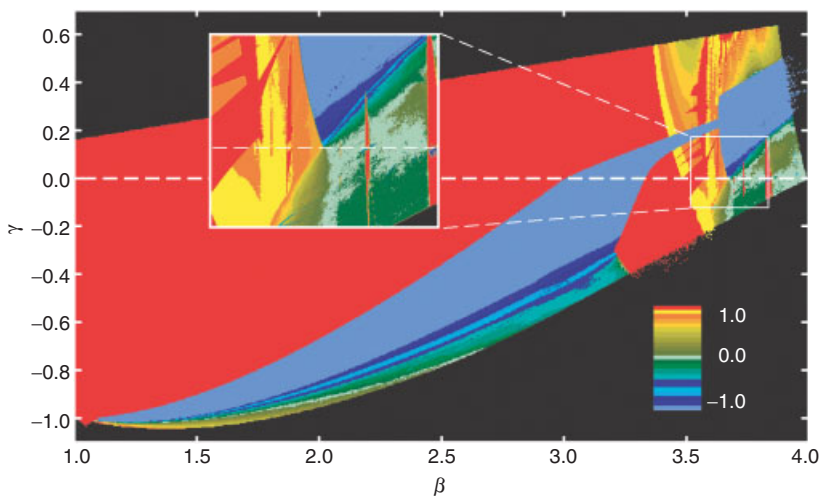

Plate 4. Cross correlation $\overline{u'v'}$ as function of β and γ.

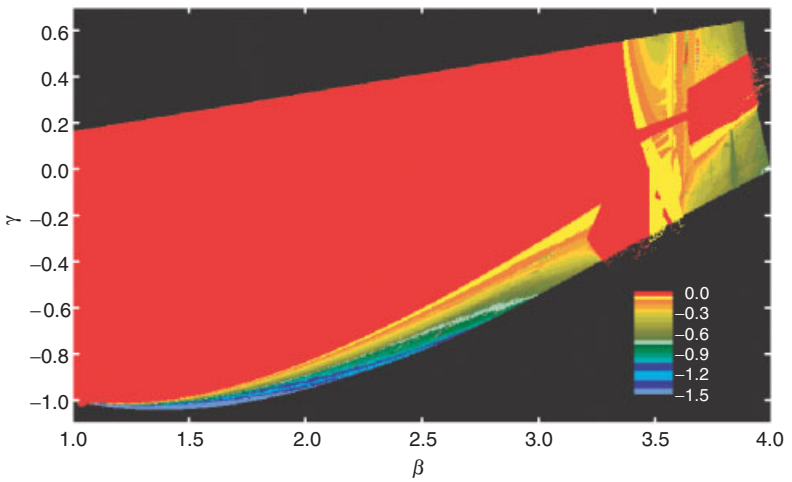

Plate 5. Skewness of $\mathrm{d}u/\mathrm{d}t$ as function of β and γ.

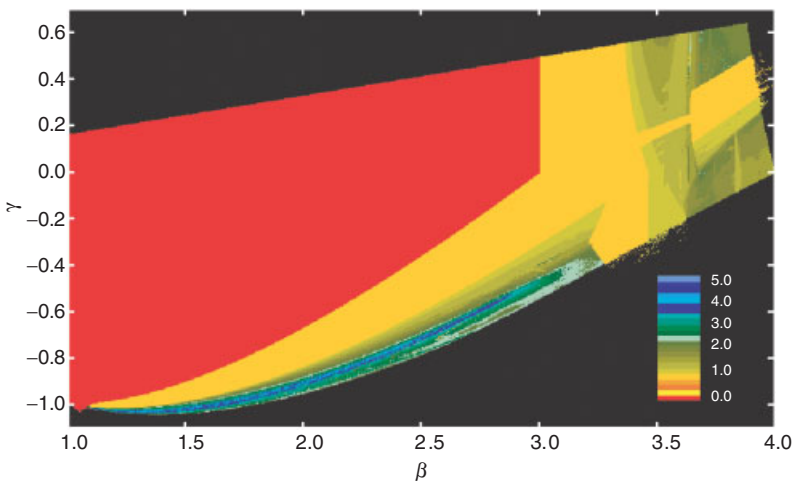

Plate 6. Flatness of u as function of β and γ.